Journal of Nanobiotechnology

RESEARCH

Open Access

aPD-L1-facilitated theranostic and tumor microenvironment remodeling of pancreatic cancer via docetaxel-loaded phase-transformation nanoparticles triggered by low-intensity pulsed ultrasound

Yi Tang[1,2†], Qingling Shen[1,2†], Peng Lin[1], Zhixin Chen[3], Denghui Fan[4], Minling Zhuo[1], Yajiao Gan[1], Yixi Su[1], Qingfu Qian[1], Liwu Lin[1], Ensheng Xue[1] and Zhikui Chen[1,2*]

Abstract

Early diagnosis of pancreatic ductal adenocarcinoma (PDAC) is challenging because of its depth, which often leads to misdiagnosis during ultrasound examinations. The unique PDAC tumor microenvironment (TME) is characterized by significant fibrous tissue growth, and high interstitial pressure hinders drug penetration into tumors. Additionally, hypoxia and immune suppression within the tumor contribute to poor responses to radiotherapy and chemotherapy, ultimately leading to an unfavorable prognosis. In this study, aPD-L1-modified docetaxel and perfluoropentane-loaded liquid–vapor phase-transformation lipid nanoparticles (aPDL1-DTX/PFP@Lipid) were synthesized and had an average diameter of 61.63 nm with 84.3% antibody modification. We demonstrated that the nanoparticles (NPs) exhibited excellent PDAC-targeting capabilities both in vitro and in vivo. Upon exposure to low-intensity pulsed ultrasound (LIPUS) stimulation, the NPs underwent a phase transformation to form microbubbles with substantial molecular ultrasound diagnostic effects, and combined treatment resulted in a tumor growth inhibition rate of 88.91%. This treatment strategy also led to the infiltration of $CD8^+$ T cells, the downregulation of Treg cells, the promotion of M1 macrophage polarization, the inhibition of fibrosis to reduce tumor stromal pressure, and the facilitation of perfluoropentane (PFP) gasification to release O_2 and improve tumor hypoxia. In conclusion, aPD-L1-modified liquid–vapor phase-transformation nanoparticles loaded with docetaxel (DTX) and PFP were successfully combined with ultrasound for the molecular diagnosis and targeted treatment of PDAC. aPDL1-DTX/PFP@Lipid could reshape the PDAC TME, offering a new approach for ultrasound-mediated diagnosis and treatment with promising clinical applications.

†Yi Tang and Qingling Shen contributed equally to this work.

*Correspondence:
Zhikui Chen
jimchen2003@163.com

Full list of author information is available at the end of the article

Keywords Contrast-enhanced ultrasound, Molecular diagnosis, Targeted therapy, Tumor microenvironment, Pancreatic cancer

Graphical Abstract

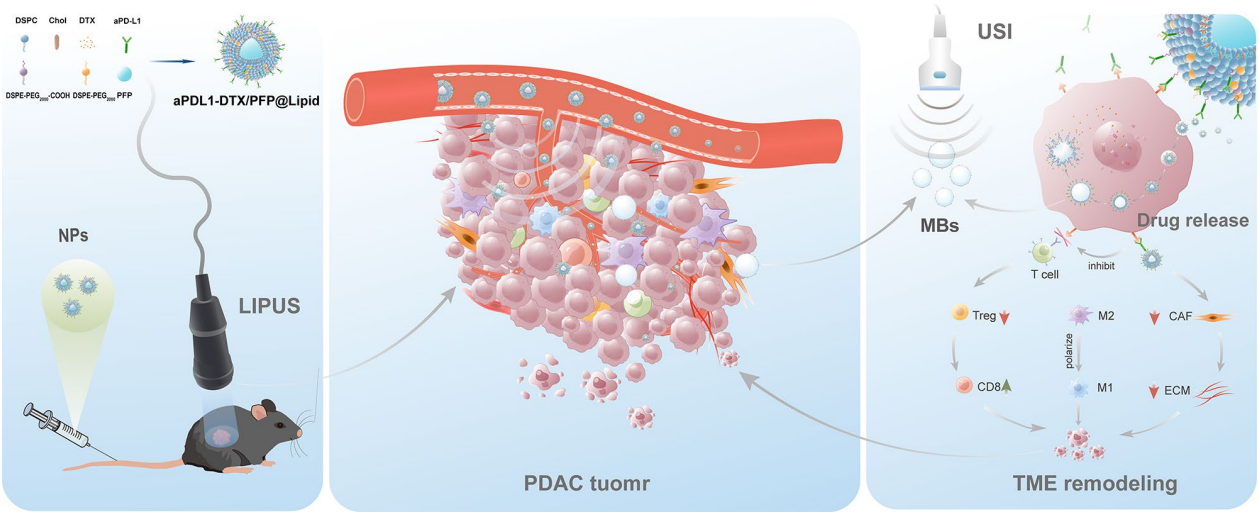

Introduction

In recent years, the incidence of pancreatic cancer (PDAC) has been steadily increasing at a rate of 0.5–1% annually [1, 2]. PDAC is insidious at disease onset, challenging to diagnose in the early stages, and often is diagnosed in advanced stages, which results in a missed window for surgical resection. The tumor microenvironment (TME) is characterized by immune evasion, hypoxia, and high stromal pressure, which hinder drug delivery, resulting in poor responses to immunotherapy and chemotherapy [3]. Owing to the highly invasive nature and poor prognosis of PDAC, the 5-year survival rate of patients in China decreased from 11.7% from 2003 to 2005 to 7.2% from 2012 to 2015, which is the lowest among all cancer-related survival rates [4]. Hence, there is an urgent clinical need to address the current challenges in the clinical diagnosis and treatment of PDAC by developing a sensitive method that can detect PDAC at an early stage and achieve efficient drug delivery.

The depth of the pancreas and its location behind the peritoneum and the presence of gastrointestinal gas pose challenges during abdominal ultrasound examinations. Furthermore, other factors, such as examiner experience and skill, have historically restricted the clinical effectiveness of abdominal ultrasound. Despite the increased clinical use of contrast-enhanced ultrasound (CEUS) imaging techniques in recent years, the resolution of pancreatic imaging remains inadequate. CEUS is a dynamic, continuous process that lasts approximately three minutes, during which time gas interference can compromise the quality of contrast enhancement, leading to suboptimal diagnostic outcomes. Additionally, the average particle size of a microbubble contrast agent used in CEUS is approximately 2.6 μm [5], which hinders the ability of the contrast agent to traverse endothelial gaps, bind selectively to cancer cells, and consequently perform targeted tumor diagnosis [6].

Advances in molecular ultrasound imaging have opened new possibilities for the diagnosis and treatment of tumors [7]. The small size of liquid–vapor phase-transformation nanoparticles allows them to easily penetrate tumor blood vessels and bind specifically to cancer cells. These nanoparticles (NPs) can be converted into microbubbles (MBs), which improve ultrasonography imaging quality by inducing a phase change through the application of heat or ultrasound irradiation. This noninvasive approach enables the visual diagnosis of tumor biological behaviors at the cellular and subcellular levels [8–10]. Upon triggering a phase change in the NPs, the encapsulated perfluoropentane (PFP) is gasified to release O_2, leading to an increase in reactive oxygen species (ROS) production in tumor cells [11]. Moreover, MBs rupture by ultrasound-targeted microbubble destruction (UTMD) generates ultrasound-induced biological effects that increase the permeability of cancer cell membranes, aiding drug entry into cancer cells, improving drug delivery efficiency, and improving treatment outcomes [12–14].

In this study, we propose the construction of aPD-L1-modified docetaxel and perfluoropentane-loaded liquid–vapor phase-transformation lipid nanoparticles (aPDL1-DTX/PFP@Lipid) (Scheme 1). These small NPs are designed to effectively target PDAC cells by penetrating the blood vessel wall. Upon exposure to low-intensity

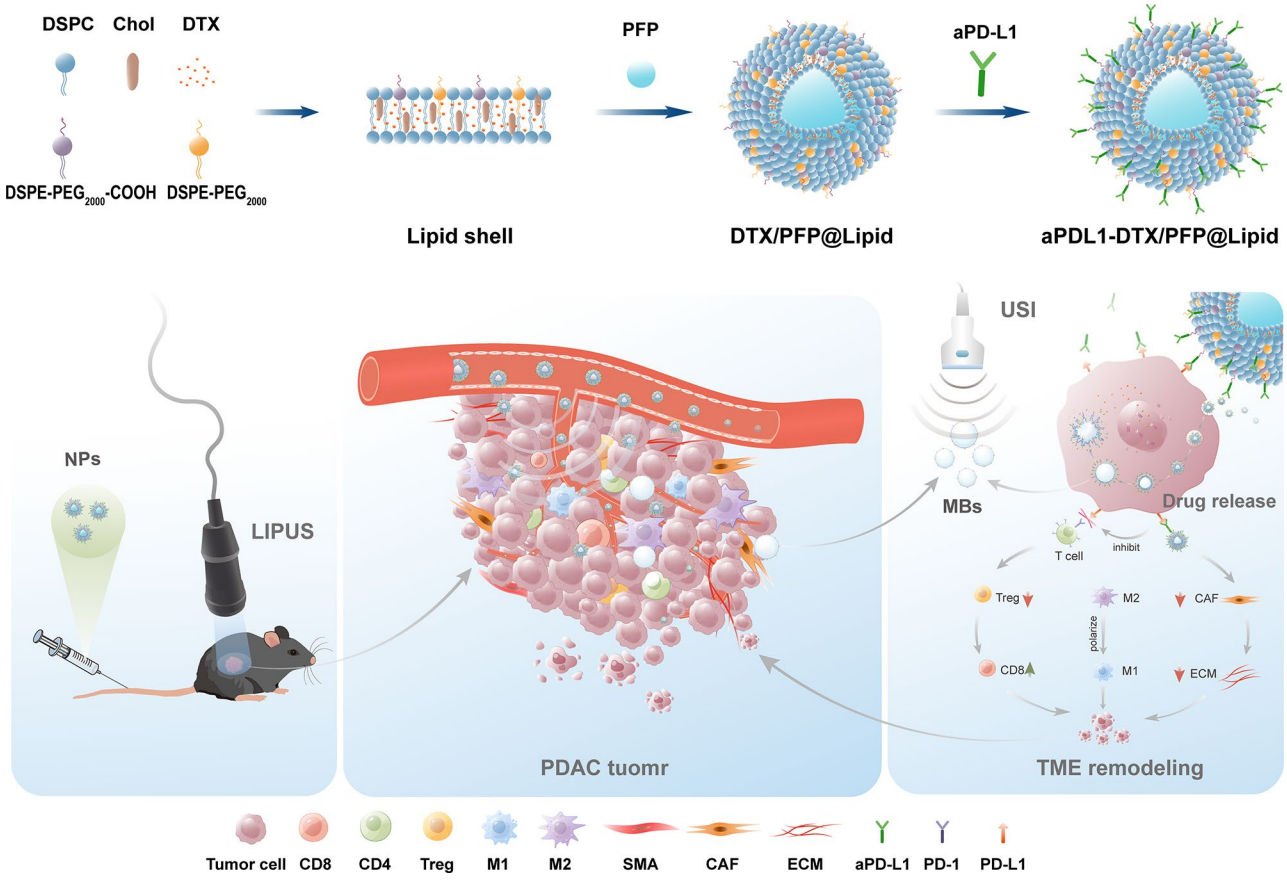

Scheme 1 Schematic illustration of the production of aPDL1-DTX/PFP@Lipid and how they are used in PDAC-bearing mice in vivo

pulsed ultrasound (LIPUS), the NPs undergo a phase change, enabling molecular diagnosis via ultrasonography. The physical effects induced by UTMD can directly harm cancer cells, while an anti-PD-L1 antibody (aPD-L1) and docetaxel (DTX) are simultaneously delivered for immunotherapy and chemotherapy. Moreover, the PFP transported by the nanoparticles acts as an oxygen reservoir to improve the hypoxic conditions in the PDAC TME. This comprehensive strategy alters the PDAC TME in multiple ways, resulting in integrated molecular ultrasound diagnosis and targeted therapy for PDAC.

Methods

Materials and animals

The following reagents were used in this study: 1,2-distearoyl-sn-glycero-3-phosphocholine (DSPC), 1,2-distearoyl-sn-glycero-3-phosphoethanolamine-N- [methoxy(ethylene glycol)-2000] (DSPE-PEG_{2000}) (AVT Pharmaceutical, China), 1,2-distearoyl-sn-glycero-3-phosphoethanolamine-N-[carboxy(polyethylene glycol)-2000] (DSPE-PEG_{2000}-COOH) (Xi'an Ruixi Biological Technology, China),

cholesterol (Sigma, USA), docetaxel (J&K Scientific, China), anti-mouse PD-L1 antibody (#HY-P99145, MedChemExpress, USA), rabbit anti-mouse CD8 antibody (#ab217344, Abcam, UK), Ki67 monoclonal antibody (SolA15) (Invitrogen, USA), rabbit anti-α-smooth muscle actin (α-SMA) antibody (#ET1607-53, HUABIO, China), pancytokeratin (Pan CK) monoclonal antibody Alexa Fluor™ 488 (#53-9003-82), donkey anti-rabbit IgG (H + L) highly cross-adsorbed secondary antibody Alexa Fluor™ 568 (#A10042), and donkey anti-mouse IgG (H + L) highly cross-adsorbed secondary antibody Alexa Fluor™ 647 (#A-31573) (Thermo Fisher, USA) were used.

Mouse PDAC cells (Pan02) were purchased from the National Experimental Cell Resource Sharing Platform (Beijing, China). C57BL/6 mice (4 weeks; 18–22 g) and SD rats (300–350 g) were obtained from Silaike Experimental Animal Co., Limited Liability Company (Shanghai, China).

Synthesis of the targeted DTX-loaded phase-transformation NPs

DSPC, DSPE-PEG_{2000}, cholesterol, poloxamer, and DSPE-PEG_{2000}-COOH were dissolved at a mass ratio of 20 mg:3 mg:1 mg:1.8 mg:2.5 mg in 2 mL of trichloromethane.

Five milligrams of docetaxel was dissolved in 1 mL of methanol and added to this mixture. The solvent was then evaporated via vacuum rotary evaporation in a water bath at 50 °C for 30 min to form a DTX-loaded phospholipid mixture film. The film was subsequently hydrated with 4 mL of MES buffer (0.1 M, *pH 6*) by ultrasonic dispersion at 300 W in a water bath at 50 °C to create a phospholipid suspension.

To obtain docetaxel and perfluoropentane-loaded liquid–vapor phase-transformation lipid nanoparticles (DTX/PFP@Lipid), 1 mL of the phospholipid suspension was mixed with 15 μL of PFP and emulsified via non-contact ultrasonication (XM08-II, Xiaomei Ultrasonic Instruments) for 10 min (1000 W, 30 s on/off) in a water bath at 3 °C. Uniformly, perfluoropentane-loaded liquid–vapor phase-transformation lipid nanoparticles (PFP@Lipid) are prepared using a phospholipid suspension without DTX.

The carbodiimide method was used to modify the nanoparticles. A solution of 1-ethyl-3-(3-dimethylaminopropyl)carbodiimide/N-hydroxysuccinimide (EDC/NHS) in MES buffer (0.1 M, *pH 6*) was prepared and added to DTX/PFP@Lipid (-COOH: EDC: NHS = 1:10:30, molar ratio) for 2 h at 4 °C to activate the carboxyl groups, followed by ultrafiltration and centrifugation for 2 h (4 °C, 6000 rpm) to remove the buffer and excess EDC/NHS.

Finally, the activated DTX/PFP@Lipid mixture was resuspended in MES buffer (0.1 M, *pH 8*), and aPD-L1 was introduced at a DTX: aPD-L1 mass ratio of 6:1. After thorough mixing, the mixture was incubated at 4 °C with slow shaking for 2 h to obtain aPDL1-DTX/PFP@Lipid.

Characterization of the NPs

A copper mesh with Formvar® film was coated by the dropwise addition of 20 μL of aPDL1-DTX/PFP@Lipid (diluted 1:500 in ultrapure water), and after 15 min of adsorption, the sample was negatively stained with 2% (W/V) phosphotungstic acid (*pH 6.5*) for 30 s. The internal structure and morphology of the nanoparticles were observed via transmission electron microscopy (TEM) (HT7700, Hitachi). The particle size distribution, zeta potential, and polydispersity index (PDI) of the NPs were determined with a particle size analyzer (LitesizerTM 500, Anton Paar), and these measurements were repeated on days 1, 5, and 10 following preparation to assess the in vitro stability of the nanoparticles.

After lyophilization, Fourier transform infrared (FTIR) spectra of PFP@Lipid, DTX, DTX/PFP@Lipid, aPDL1-DTX/PFP@Lipid, and aPD-L1 were collected on a Nicolet is50 infrared spectrometer (Thermo Fisher Scientific, Waltham, MA, USA) by scanning the infrared range from 400 to 4,000 cm^{-1}.

Encapsulation efficiency (EE) and drug loading capacity (LC) of the NPs

Liquid chromatography–tandem mass spectrometry (LC–MS/MS) (Triple Quad™ 4500, Applied Biosystems & LC–30AC, Shimadzu) was used to determine the EE and LC of DTX in the drug-loaded phase-transformation nanoparticles. The chromatographic column used was a Shim-pack GSP-HPLC C18 column (3 μm, 2.1 mm × 50 mm). Mobile phase A (aqueous phase) was an aqueous solution of 0.1% formic acid, while mobile phase B (organic phase) consisted of 0.1% formic acid in acetonitrile. Gradient elution was performed with a column temperature of 40 °C, an injector temperature of 8 °C, an injection volume of 4 μL, and a flow rate of 0.6 mL/min. Additionally, the electrospray ionization source was operated in positive ion mode via multiple reaction monitoring (MRM). The ion source settings were as follows: voltage, 5.5 kV; temperature, 500 °C; air curtain gas, 35 psi; spray gas, 50 psi; and auxiliary heating gas, 50 psi. The mass transition of DTX from 830.5→549.3 m/s was quantified with a declustering potential (DP) of 140 V and a collision energy (CE) of 60 V.

$$\mathrm{EE}\,(\%) = \left(\frac{\text{DTX content in the NPs}}{\text{total amount of DTX delivered}}\right) \times 100\%$$

$$\mathrm{LC}\,(\%) = \left(\frac{\text{DTX content in the NPs}}{\text{total mass of the NPs}}\right) \times 100\%$$

Determination of aPD-L1 modification efficiency

DiI-labeled aPDL1-DTX/PFP@Lipid was mixed with 1 mL of PBS and 2 μL of donkey anti-mouse IgG (H + L) Alexa Fluor Plus 488 (#A32766, Thermo Fisher) and incubated for 2 h at 4 °C. The mixture was then centrifuged at high speed (14,000 rpm, 4 °C) to eliminate any unbound secondary antibody. The sample was subsequently washed three times with PBS, after which the dual fluorescently labeled NPs were suspended in ultrapure water. Fluorescence images were captured with a Leica DMi8 fluorescence microscope, and image colocalization was analyzed with Leica application suite X 3.5.7 (LAS X) software. The rate of aPD-L1 conjugation to DTX/PFP@Lipid was assessed by flow cytometry (BD Accuri C6 Plus), and quantitative analysis was performed with FlowJo 10.8.1 software.

Evaluation of drug release in vitro and in vivo

In vitro experiments employed dialysis to analyze the release profile of DTX from aPDL1-DTX/PFP@Lipid. The 1 mL DTX-loaded NPs were sealed in dialysis bags (MWCO 8–14 kDa) and dialyzed in PBS buffer solution (100 mL, pH 7.4) containing 0.1% (w/v) Tween 80 at 4 °C with constant stirring [15, 16]. At various time points

(1 h, 2 h, 4 h, 6 h, 12 h, 24 h, 48 h, 72 h, 96 h, 120 h, 144 h, 168 h, and 192 h), 300 μL of dialysate was collected and promptly replenished with 300 μL of fresh PBS to maintain a constant volume. The DTX reference standard was diluted with blank PBS buffer as the matrix to prepare the working solutions for the standard curve and the quality control samples. The concentration of DTX in the buffer at each time point was analyzed by LC–MS/MS via the same detection method as previously described.

The in vivo release efficiency of DTX was studied in SD rats. DTX-loaded NPs (DTX: 3.5 mg/kg) were intravenously administered to normal SD rats ($n = 4$), peripheral anticoagulated blood was collected from the tail vein at various time points (1 h, 2 h, 4 h, 6 h, 12 h, 24 h, 48 h, 72 h, 96 h, 120 h, 144 h, 168 h, and 192 h), and 200 μL of plasma sample was collected after high-speed centrifugation (10 000 rpm, 10 min). The DTX reference standard was diluted with blank plasma as the matrix to prepare the working solutions for the standard curve and the quality control samples, and the DTX concentrations in the plasma were analyzed via LC–MS/MS.

Thermotropic capability of the liquid–vapor phase-transformation NPs

The NPs solution was diluted to a concentration of 0.5 mg/mL with double-distilled water and placed in transparent flat-bottom glass vials. These vials were then heated in a water bath at 37 °C, 40 °C, 45 °C, 50 °C, 55 °C and 60 °C for 5 min at each temperature. The number and morphology of the phase-transformation MBs were determined under an optical microscope (CKX41, Olympus). Three random fields of view were chosen from each group for image capture, and the numbers and diameters of the MBs were assessed by ImageJ for statistical analysis.

Acoustic droplet vaporization (ADV) and ultrasound imaging of the NPs in vitro

The aim of this study was to investigate the effects of thermal and LIPUS in vitro-triggered ADV on ultrasound imaging signal enhancement. First, 1 mL of aPDL1-DTX/PFP@Lipid diluted in double-distilled water was added to centrifuge tubes and heated in a water bath at temperatures ranging from 37 °C to 60 °C for 5 min at each temperature. B-mode and CEUS images of the nanoemulsions in the centrifuge tubes were acquired at various temperatures with a Canon i800 diagnostic ultrasound instrument equipped with a line array probe (model: i18LX5, center frequency: 12 MHz).

Subsequently, 1 mL of NPs (50 μg/mL) was added to a centrifuge tube to determine the effects of duration (1–5 min) and acoustic intensity (0.5, 1.0, 1.5, 2, 2.0, 2.5 W/cm^2) on the ADV induced by LIPUS stimulation of the NPs in vitro. Ultrasound images of the nanoparticle emulsions in the centrifuge tubes were captured after each irradiation session with a Canon i800 diagnostic ultrasound device equipped with an i18LX5 line array probe. The CEUS signal intensity values and B-mode image grayscale values were quantified with the device's integrated TCA software and ImageJ.

Confirmation of PD-L1 expression in Pan02 cells

Pan02 cells were seeded at a density of 1×10^5 cells per well in 96-well plates and cultured at 37 °C in a humidified incubator with 5% CO_2. Upon reaching 60% confluence, the culture medium was aspirated, and the cells were fixed with 4% paraformaldehyde at room temperature. After being rinsed three times with phosphate-buffered saline (PBS), the cells were blocked with bovine serum albumin (BSA) for 30 min. A rabbit anti-mouse PD-L1 antibody (#ab213480, Abcam, 1:500) was subsequently added, and the samples were incubated for 1 h at 37 °C, followed by three additional washes with PBS. Next, goat anti-rabbit IgG-FITC (ab6717, Abcam, 1:500) was applied, and the samples were incubated for 30 min at 37 °C in the dark prior to washing three times with PBS. The cells were then stained with DAPI staining solution, incubated for 10 min at room temperature in darkness, and washed with PBS, after which the fluorescence of FITC on the surface of the Pan02 cells was visualized with a fluorescence microscope.

Pan02 cells in the logarithmic growth stage were harvested, fixed with 4% paraformaldehyde for 15 min, and washed three times with PBS. After the cell density was adjusted to 2×10^6/mL, 500 μL of the cell suspension was incubated with 2 μL of anti-mouse PD-L1 antibody at 37 °C for 1 h in the dark, followed by centrifugation at 1000 rpm for 5 min and resuspension of the cells in 500 μL of PBS. Next, goat anti-rabbit IgG-FITC was added, and the cells were incubated on a shaker at 37 °C for 30 min. After an additional centrifugation step and three washes, the Pan02 cells were resuspended in 500 μL of PBS and analyzed by flow cytometry.

Targeting efficiency of aPDL1-DTX/PFP@Lipid in vitro

Pan02 cells were placed in 96-well plates at predetermined concentrations and incubated for 24 h, after which the medium was discarded. Serum-free DMEM was then added for an additional 4 h of culture. Next, the cells were divided into three groups: nontargeting, targeting, and antagonist. In the antagonist group, an excess of anti-mouse PD-L1 antibody was introduced 30 min before the end of the starvation culture. Next, 10 μL of DiI-labeled DTX/PFP@Lipid or aPDL1-DTX/PFP@Lipid (2 mg/mL) was added to each group after the starvation culture was complete, and the cells were incubated for an additional 2 h. The culture medium was then withdrawn, any unbound nanoparticles were removed by thorough

washing with PBS, and the cells were fixed in 4% paraformaldehyde and stained with DAPI solution. Finally, the cells were washed with PBS three times and observed under a fluorescence microscope.

NPs uptake by Pan02 cells in vitro

Pan02 cells in the logarithmic growth phase were seeded at a density of 1×10^5 cells per well in 96-well plates and allowed to adhere. Subsequently, 10 μL of DiI-labeled aPDL1-DTX/PFP@Lipid was added for coculture in the dark for 3, 6, 9, or 12 h. The cells were then rinsed with PBS, fixed with 4% paraformaldehyde, stained with DAPI solution, and observed under a fluorescence microscope.

Similarly, Pan02 cells were seeded in 12-well plates and cultured until they reached confluence. The cells were then cocultured with 100 μL of DiI-labeled aPDL1-DTX/PFP@Lipid for various durations (0, 3, 6, 9, or 12 h). The culture medium containing the nanoparticles was removed, the cells were washed three times with PBS, and cell pellets were obtained following trypsin digestion and centrifugation. After three additional washes with PBS, the cell concentration was adjusted, and the cells were analyzed by flow cytometry.

Detection of ROS production and NPs cytotoxicity

Pan02 cells were seeded in 48-well plates and divided into four groups: control, NPs, LIPUS, and NPs + LIPUS. The NPs and NPs + LIPUS groups were treated with 10 μL of aPDL1-DTX/PFP@Lipid for 6 h after cell attachment and ultrasonic irradiation (2.5 W/cm^2, 3 min), followed by the LIPUS and NPs + LIPUS groups. The cells were subsequently cultured for an additional 24 h. The intracellular ROS levels were detected with an ROS fluorescence assay kit (#E-BC-K138-F, Elabscience), and the cell nuclei were labeled with Hoechst 33,342 (#62249, Thermo Scientific).

The cytotoxicity of the NPs was assessed via CCK-8 assays. The cells were seeded at a density of 1×10^5 cells per well in 96-well plates and divided into the following groups: free DTX, PFP@Lipid, DTX/PFP@Lipid, and aPDL1-DTX/PFP@Lipid ($n = 3$). Different concentrations of DTX (1.25 μg/mL, 2.5 μg/mL, 6.25 μg/mL, 12.5 μg/mL, and 25 μg/mL) were evaluated, with PFP@Lipid without DTX or aPD-L1 serving as control nanoparticles. Each group was further divided into ultrasonication-irradiation and no ultrasonication subgroups. Following 6 h of incubation after drug addition, the ultrasonication-irradiation subgroups were subjected to LIPUS irradiation (2.5 W/cm^2, 3 min) and incubated for an additional 24 h. The culture medium was subsequently aspirated, the cells were washed with PBS, and fresh medium containing 10% CCK-8 was added to the wells for an additional 0.5–1 h of incubation. The OD at 450 nm was measured with a multifunctional enzyme reader (SpectraMax i3X, Molecular Devices).

Chemotaxis and immunocytotoxicity of CD8$^+$ T cells in vitro

Isolation and activation of murine CD8$^+$ T cells: CD8$^+$ T cells were isolated from mouse spleens via a Mouse CD8$^+$ T-Cell Isolation Kit (# CS103-01, Vazyme) following the manufacturer's protocol. To activate the T cells, anti-mouse CD3 (# AM003E, MultiSciences) and anti-mouse CD28 (# AM028, MultiSciences) antibodies were utilized.

T-cell chemotaxis assay: CD8$^+$ T cells were then seeded into 3 μm pore-sized Transwell chambers (Cat# 3422, Corning) at a density of 1×10^5 cells per insert and cocultured with supernatants from various treatment groups. After a 24 h incubation period, the cells that had migrated to the lower compartment were collected and counted.

Cytotoxicity assay: Cells from each treatment group were enumerated and plated at a density of 1×10^4 cells per well in a 96-well plate. Activated T cells, also at a density of 1×10^4 cells per well, were cocultured with tumor cells. After 24 h, the cytotoxic effects were assessed via a CCK-8 assay kit (# CK04, Dojindo) according to the manufacturer's instructions.

NPs biodistribution in vivo

A suspension of Pan02 cells in the logarithmic growth phase was combined with an equal proportion of cell matrix gel (#354234, BD BioCoat) under cold conditions. Then, 0.2 mL (1×10^7 cells) of the suspension was injected into the right inguinal subcutis of each C57BL/6 mouse. The tumor was considered ready for the experiment once it reached a diameter of 1 cm. Prior to the experiment, the tumor-bearing mice were shaved such that the abdomen and tumor site were completely exposed. The mice were subsequently randomly assigned to two groups: the nontargeting group and the aPD-L1-targeting group ($n = 5$). DiR-labeled NPs (200 μL) were injected into the mice in both groups via the tail vein, and images were captured from the mice under continuous isoflurane anesthesia at specific time points (2 h, 6 h, 12 h, 24 h, 48 h, 96 h, and 192 h postinjection) with a small animal in vivo fluorescence imaging system (IVIS® Spectrum, Caliper Life Sciences). The excitation and emission wavelengths used were 740 nm and 780 nm, respectively. The fluorescence signal intensity was quantitatively assessed with Living Image.

Furthermore, the tumor-bearing mice were euthanized at 6 h or 24 h after intravenous injection of the NPs. The major organs, including the heart, liver, spleen, lungs, kidneys, and tumors, were subsequently isolated for fluorescence imaging to assess the distribution of the fluorescence signal.

Phase transformation of the NPs in vivo and ultrasound imaging

Nine tumor-bearing mice with tumors measuring approximately 1 cm in diameter were selected for the experiment. The mice were intravenously injected with 200 μL of DTX/PFP@Lipid, aPDL1-DTX/PFP@Lipid, or PBS (control group) ($n = 3$). At 6 h and 24 h postinjection, the mice were anesthetized with 400 mg/kg tribromoethanol via intraperitoneal administration. The tumor site was subsequently exposed to LIPUS irradiation (2.5 W/cm^2, 3 min). Ultrasound images were captured with a Canon i800 diagnostic ultrasound instrument with an i18LX5 line array probe at the following time points: preinjection and 6 h postinjection + LIPUS and 24 h postinjection + LIPUS, after which the B-mode and CEUS image signal intensities were analyzed.

Evaluation of the in vivo antitumor efficacy of combined NPs and LIPUS treatment

Pan02 cells were inoculated into the right abdominal subcutis of the mice. When the tumor volume reached approximately 60 mm^3, the mice were randomly divided into 7 groups ($n = 5$): model, ultrasound irradiation alone, free DTX, free aPD-L1, DTX/PFP@Lipid, aPDL1-DTX/PFP@Lipid, DTX/PFP@Lipid + LIPUS, and aPDL1-DTX/PFP@Lipid + LIPUS. The NPs or free drugs were injected at the same dose (DTX: 30 mg/kg; aPD-L1: 5 mg/kg) via the tail vein. Twenty-four hours after intravenous drug administration, the tumor site was irradiated with LIPUS (2.5 W/cm^2, 5 min). The treatment was repeated every 5 days for a total of 3 times. Tumor growth was monitored regularly. After 1 week of observation following the last treatment, the mice were euthanized by cervical dislocation, and the tumors were removed and weighed to calculate the relative rate of tumor growth inhibition, as follows.

$$\text{Inhibition rate } (\%) = \left(1 - \frac{\text{tumor mass of experimental group}}{\text{tumor mass of control group}}\right) \times 100$$

Histopathological and immunohistochemical analyses of tumor tissues

Each tumor sample was fixed in tissue fixative, dehydrated, embedded in paraffin, and then cut into serial Sect (4 μm thick). These sections were subjected to hematoxylin and eosin (H&E) and immunofluorescence chemical staining to detect the expression of Pan CK, nuclear proliferation-associated antigen (Ki67), and α-SMA and CD8$^+$ T-cell infiltration. Additionally, immunohistochemical analysis was performed to assess FoxP3, CD206, and CD86 expression.

Statistical analyses

Statistical analysis was conducted via GraphPad Prism 9.5.1 software. The data are presented as the means ± standard deviations (SDs). Comparisons between two groups were performed via an independent samples t test, whereas one-way ANOVA was used for comparisons among more than two groups. Statistical significance was considered at $P < 0.05$, with levels of significance denoted as follows: no significance (*NS*), $^*P < 0.05$, $^{**}P < 0.01$, $^{***}P < 0.001$, and $^{****}P < 0.0001$.

Results

Characterization of the NPs

The aPDL1-DTX/PFP@Lipid had a size of 61.63 ± 0.55 nm with a narrow, positively skewed distribution, a PDI of 0.24 ± 0.01, and a zeta potential of -22.63 ± 0.87 mV (Fig. 1A). TEM revealed that these nanoparticles had a core–shell structure with a spheroidal shape, as reflected by their uniform size distribution (Fig. 1A). PFP@Lipid has an average particle size of 60.2 nm, as measured under TEM, with a thin lipid shell of approximately 8 nm that is smooth and uniform and an inner core cavity diameter of approximately 41.9 nm. With the addition of DTX, the average particle size of DTX/PFP@Lipid increases to 66 nm, the lipid shell increases to 22 nm, and the density becomes uneven, resulting in a "granular" change, whereas the inner core cavity is reduced to 31.5 nm. The average particle size of aPDL1-DTX/PFP@Lipid is 69.8 nm, with a shell thickness of 24.7 nm.

The FTIR analysis(Fig. 1B) revealed that PFP@Lipid exhibits a primary characteristic peak at 1737.8 cm^{-1} (C = O), which was located between the hydrophobic tail groups and hydrophilic head groups of the phospholipid molecules [17]. Additionally, there are three minor peaks at 2,918.7 cm^{-1}, 2,852.7 cm^{-1}, and 2,808.4 cm^{-1} (C-H$_2$). The spectrum of DTX shows characteristic absorption peaks at 1,707.8 cm^{-1} (C = O), 1,494.2 cm^{-1} (C = C) and 1,370.6 cm^{-1} (C-H) [15]. DTX/PFP@Lipid due to the mutual influence of the groups, the stretching of C = O is located primarily at 1,735.4 cm^{-1}, but it retains the 1,707.8 cm^{-1} peak (DTX). aPD-L1 has a C = O-NH absorption peak at 1,643.2 cm, and in aPDL1/DTX/PFP@Lipid, the C = O-NH peak is enhanced at 1,648.2 cm, which may be related to the introduction of the antibody, indicating that aPD-L1 has been successfully modified on the surface of DTX/PFP@Lipid [18].

Over 5 and 10 days of in vitro observation, there was a marginal decrease in particle size and a slight increase in the absolute value of the zeta potential, although these differences did not reach statistical significance ($P > 0.05$) (Fig. 1C-D). The EE and LC of DTX were determined to be 91.9% and 14.8%, respectively.

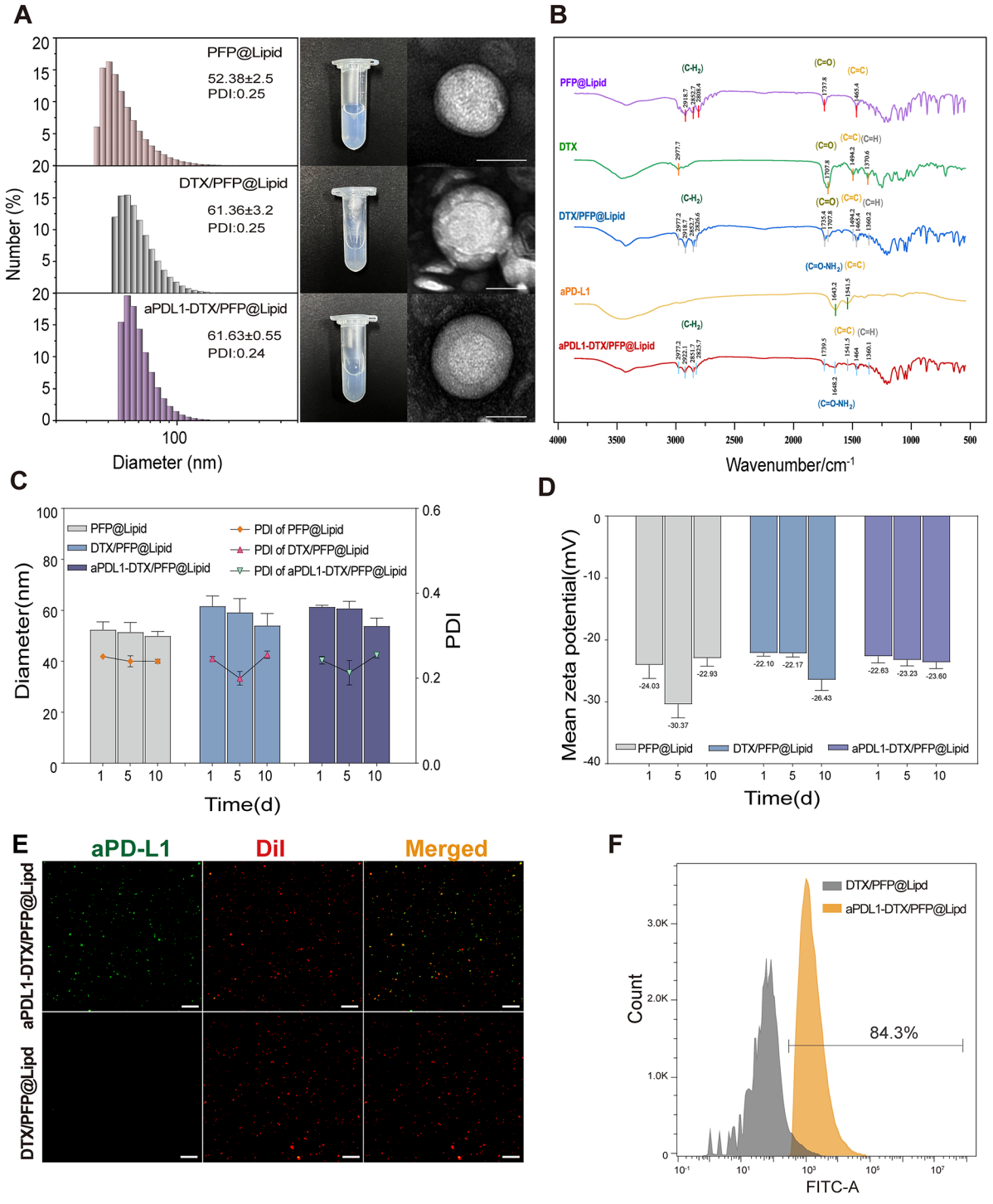

Fig. 1 NPs characterization.(**A**) The appearance and particle size distribution of the liquid–vapor phase-transformation nanoparticles and TEM image (scale bar = 50 nm).(**B**) Fourier transform infrared spectra of the NPs. (**C**) and (**D**) Dynamic comparison of particle size, PDI, and zeta potential changes among the three groups of nanoparticles on days 1, 5, and 10. (**E**) Fluorescence microscopy images demonstrating nanoparticle binding to aPD-L1, where green fluorescence indicates IgG-Alexa Fluor 488-labeled aPD-L1 and red fluorescence indicates the DiI-labeled lipid shells of the nanoparticles. (**F**) Flow cytometry analysis showing the binding of the targeted antibodies to the nanoparticles

Evaluation of drug release in vitro and in vivo

The standard curves of the DTX reference standard in the blank PBS buffer and blank plasma matrix showed good linearity within the range of 0.01–100 μg/mL, with correlation coefficients (r) of 0.9986 and 0.9982, respectively. The release rate of DTX under in vitro storage conditions gradually decreased, and the cumulative release amount was time dependent (Fig. 2A). The release rate at the first hour was 1.9%, and equilibrium was reached at approximately 156 h, with approximately 12.4% released by 192 h. In vivo studies demonstrated that the concentration of DTX in peripheral blood rapidly decreased within the initial 6 h (Fig. 2B). After standardization, the amount of DTX released from the NPs was approximately 1.1% at 1 h and reached equilibrium after 24 h in vivo, with the amount of DTX released from the blood maintained at approximately 0.1% thereafter.

In vitro phase transformation capability of the NPs

The appearance of the nanoemulsion changed from transparent to milky white as the water bath temperature increased. A gradual increase in the number of phase-transformation MBs was observed under a microscope (Fig. 3A), with a marked increase observed at 55 °C (Fig. 3B). This led to a phase transformation in which the MBs size distribution changed from sparse and uneven to small, dense, and uniform, with a diameter of approximately 7.32 ± 3.72 μm (Fig. 3C). After the phase change occurred, the volume increased 120-fold compared with that of the NPs before the phase transformation. The ultrasound echo signal intensity of the phase-transformation nanoemulsion exhibited a temperature dependence, peaking at 55 °C (Fig. 3D-E) and increasing 125-fold compared with that before the phase change. After the ultrasound-triggered phase change, the echo signal intensity of the nanoemulsion increased with increasing ultrasound irradiation intensity and time and reached the maximum intensity after 3 min of ultrasound irradiation at 2.5 W/cm^2 (Fig. 3F-G).

In vitro NPs targeting and uptake

PD-L1 expression (green fluorescence) was detected in Pan02 cells via fluorescence microscopy (Fig. 4A). Flow cytometry revealed that PD-L1 expression in Pan02 cells was approximately 96.5% (Fig. 4B). Moreover, PDAC cells exhibited significant binding to DiI-labeled aPDL1-DTX/PFP@Lipid NPs, as indicated by the red fluorescence surrounding the cells. However, NPs binding was reduced in the presence of free aPD-L1 antibody (Fig. 4C), and semiquantitative analysis of the fluorescence intensity revealed that the difference was significant ($P < 0.001$).

Furthermore, fluorescence microscopy (Fig. 5A) revealed that the cellular uptake of the nanoparticles (red fluorescence) was dependent on both intensity and time. Significant differences in the increase in fluorescence intensity were observed at the 3 h, 6 h, and 9 h time points ($P < 0.05$) (Fig. 5B). Flow cytometry analysis (Fig. 5C) confirmed that the cellular uptake efficiency of aPDL1-DTX/PFP@Lipid increased over time, with uptake rates of 15.4%, 76.1%, 91.9%, and 97.5% at 3 h, 6 h, 9 h, and 12 h, respectively.

ROS production and NPs cytotoxicity

Following combination treatment with the NPs and LIPUS irradiation, a substantial increase in the ROS signals was observed in the tumor cells (Fig. 6A). The CCK-8 results revealed a decrease in overall cell viability as the concentration of DTX or NPs increased ($P < 0.0001$). Intergroup analysis revealed that the free DTX group presented the lowest cell viability ($P < 0.001$) (Fig. 6B). After ultrasound irradiation, a significant decrease in cell viability was observed in the drug-loaded nanoparticle group, with the aPDL1-DTX/PFP@Lipid group showing the most prominent effect. At the NPs concentration of

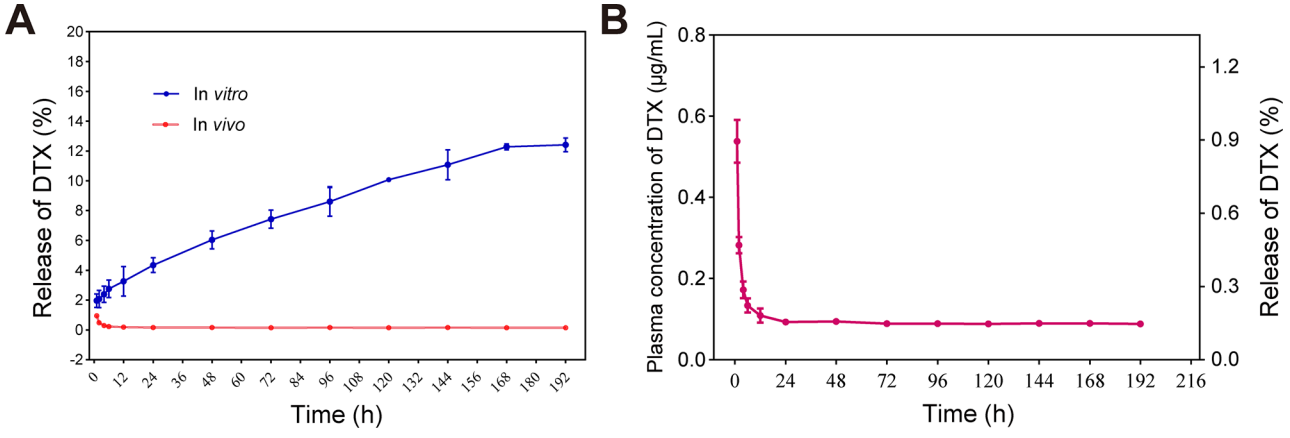

Fig. 2 DTX release profiles of DTX-loaded NPs. (**A**) Time-release percentage curves of DTX in vitro and in vivo. (**B**) Plasma concentration–time curve of DTX in vivo

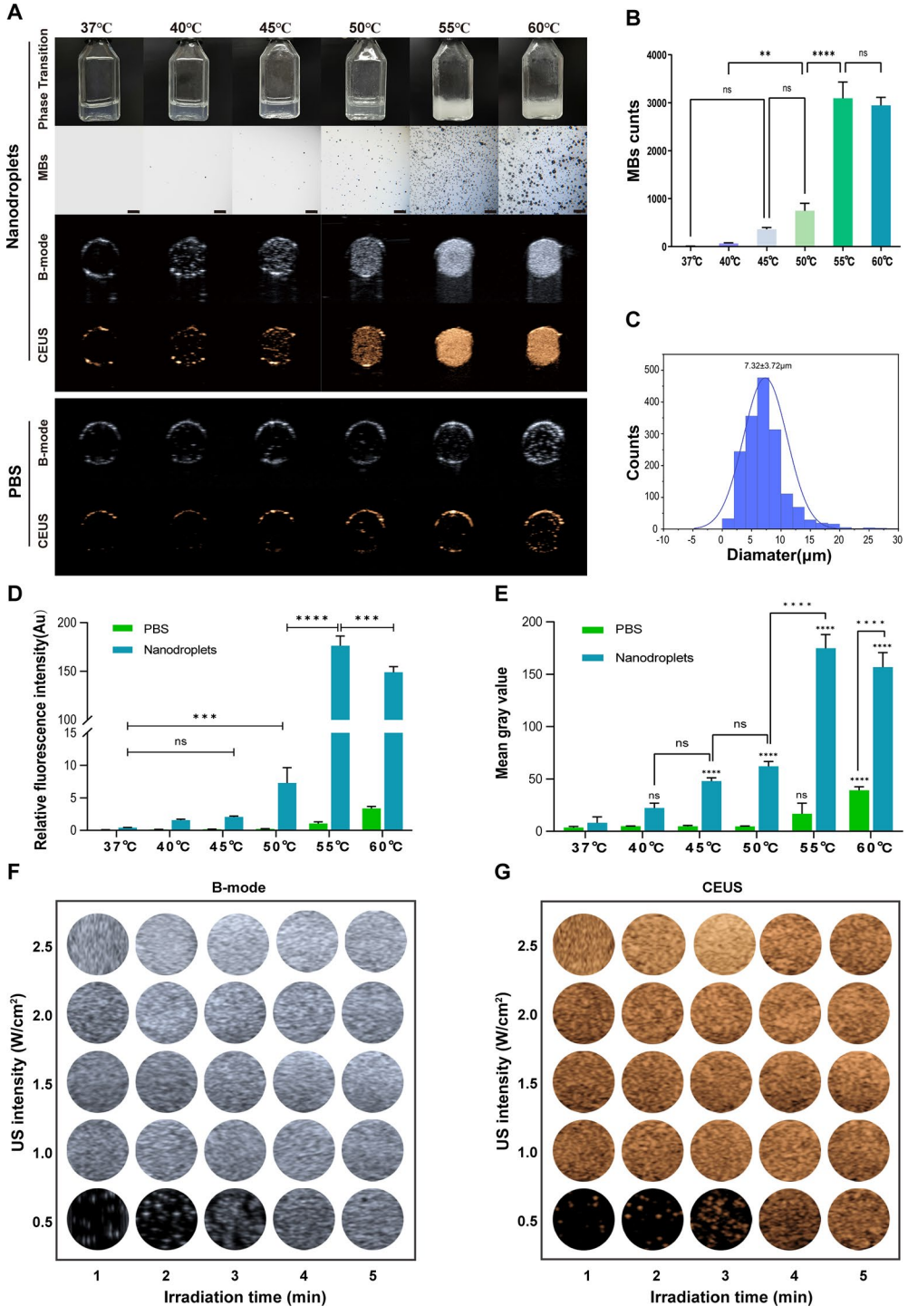

Fig. 3 In vitro phase transformation and ultrasound imaging properties of the NPs. (**A**) Optical microscopy and ultrasound images of the phase change of the thermotropic NPs (scale bar = 250 μm). (**B**) Number of phase-transformation MBs during temperature analysis. (**C**) Size distribution of the phase-transformation MBs. The gray values of the B-mode images (**D**) and the CEUS signal intensity values (**E**) of the NPs were compared with those of PBS at different temperatures. Comparison of the intensities of the B-mode images (**F**) and ultrasonography images (**G**) of the NPs with respect to the LIPUS irradiation time

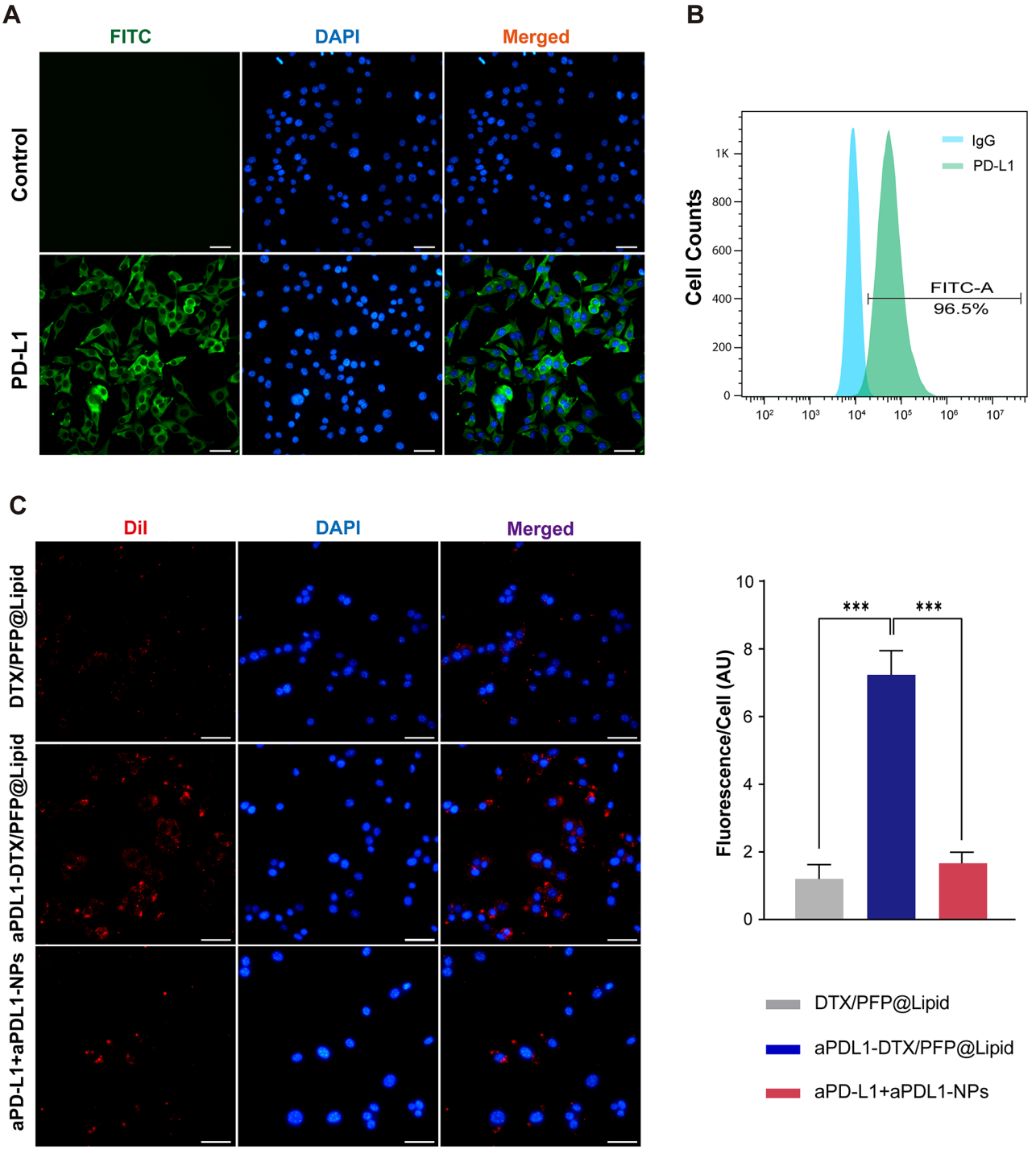

Fig. 4 In vitro cell-targeting performance of aPDL1-DTX/PFP@Lipid. Immunofluorescence (**A**) and flow cytometry (**B**) detection of PD-L1 expression in Pan02 cells (scale bar = 25 μm). (**C**) Fluorescence microscopy observations of aPDL1-DTX/PFP@Lipid binding to Pan02 cells. Red fluorescence indicates NPs labeled with DiI (scale bar = 25 μm)

25 μg/mL, the cell viability decreased to 31.14%, indicating substantial cytotoxicity ($P < 0.05$) (Fig. 6C).

NPs combined with immune cells for antitumor effects in vitro.

The in vitro cellular experiment results revealed that aPDL1-DTX/PFP@Lipid specifically binds to Pan02 cells and, after LIPUS irradiation, increases the chemotaxis of CD8 + T cells (Fig. 7B), and in combination, exerts a

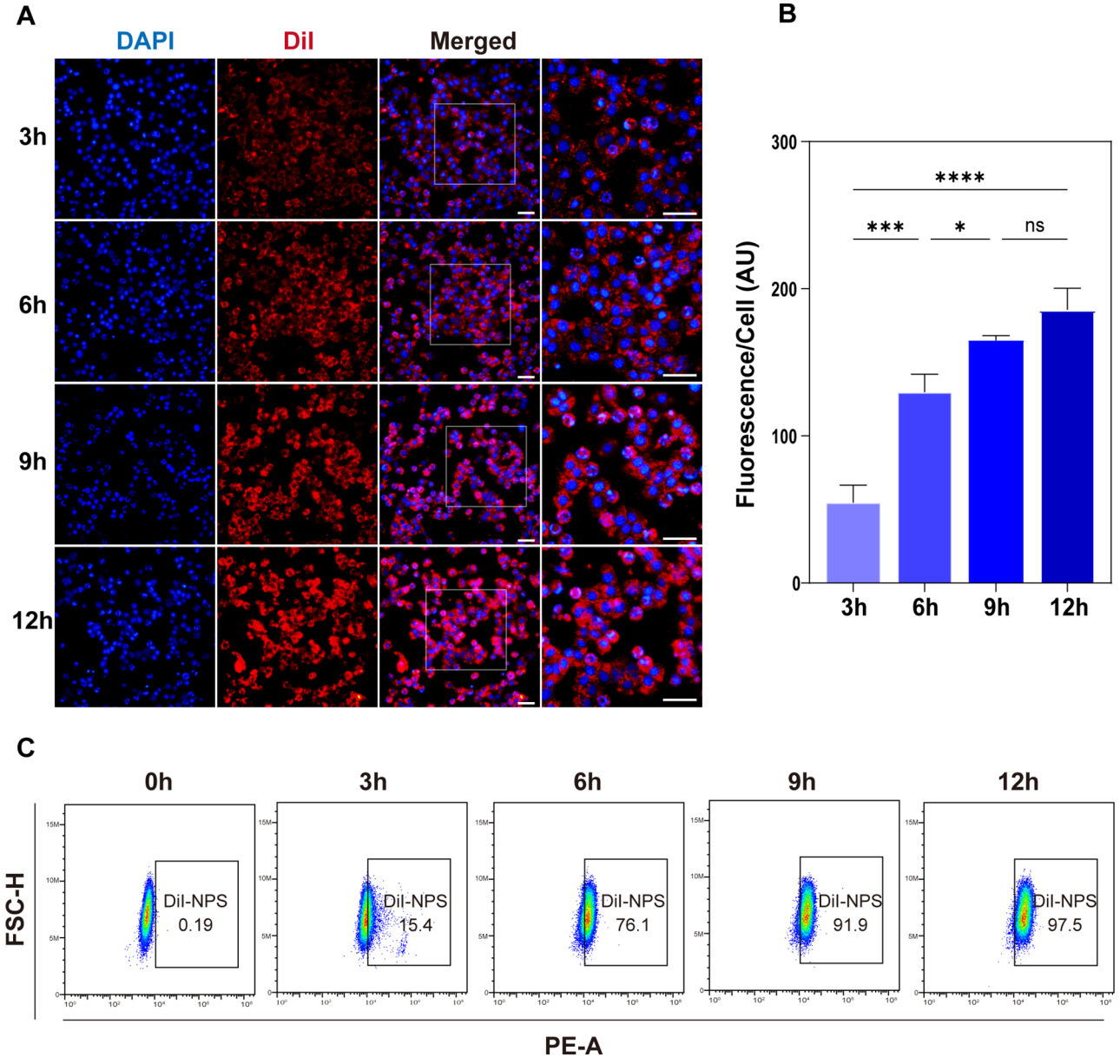

Fig. 5 Analysis of the in vitro cellular uptake efficiency of the NPs. (**A**) Fluorescence microscopy observations of Pan02 cell uptake of aPDL1-DTX/PFP@Lipid after different durations (3 h, 6 h, 9 h, and 12 h). (**B**) Analysis of fluorescence intensity. (**C**) Flow cytometry analysis of the rates of NPs uptake by cells after different durations

strong cytotoxic effect on tumor cells (Fig. 7C), with a tumor cell mortality rate of greater than 90% after 24 h.

In vivo biodistribution and metabolism of the NPs

In the targeted NPs group, the fluorescence signal intensity at the tumor site clearly and continuously increased within the first 12 h, peaked at 24 h, and then plateaued until 48 h. Clearance of the signal and a reduction in its intensity were observed at 96 h. Throughout the observation period, the fluorescence intensity in the targeted group at various time points significantly exceeded that in the nontargeted group ($P < 0.001$). Even after 192 h, the average fluorescence signal in the targeted group remained 1.85 times greater than that in the nontargeted group (Fig. 8A and C).

At 6 h and 24 h after intravenous nanoparticle injection, three mice per group were euthanized for analysis. The results showed that at 6 h, both groups presented the highest fluorescence signals in the liver and spleen, followed by the kidneys. Moreover, the tumor signal intensity in the targeted group was significantly greater than that in the nontargeted group ($P < 0.01$). By 24 h, the tumor signal intensity in the targeted group had continued to increase significantly compared with that in

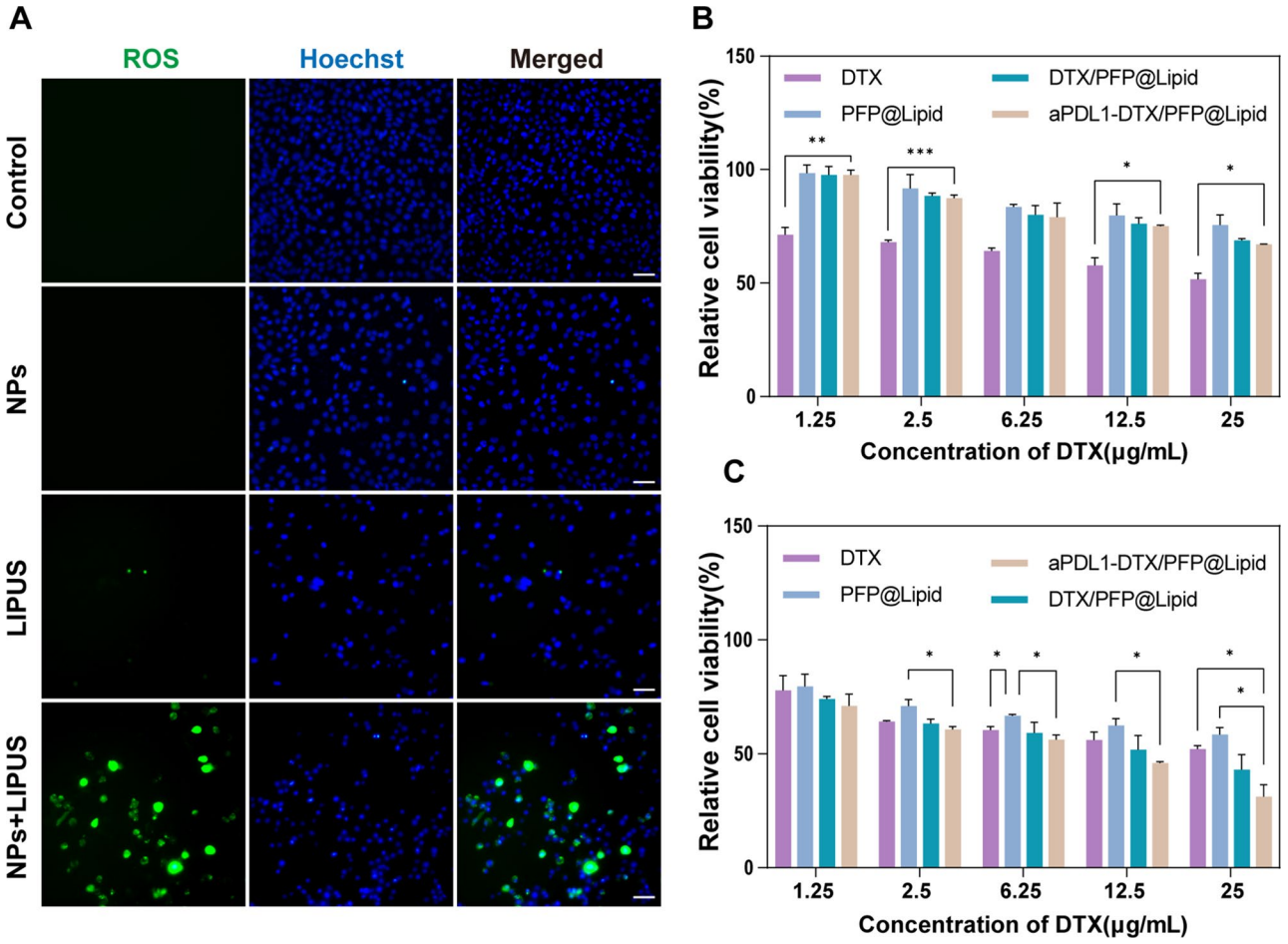

Fig. 6 Effects of the NPs on cells in vitro. (**A**) Fluorescence microscopy observations of ROS signals produced by Pan02 cells after different treatments. Pan02 cells were cultured with different concentrations of DTX and NPs without LIPUS irradiation (**B**) or with LIPUS irradiation (**C**), and cell viability was assessed

the nontargeted group ($P < 0.001$). Interestingly, analysis revealed that the fluorescence signal intensity per unit area in the tumor was significantly greater than that in the spleen ($P < 0.001$), which was a smaller difference than that in the liver ($P < 0.01$) (Fig. 8B and D).

In vivo phase transformation and ultrasound imaging of the NPs

LIPUS irradiation was performed at the tumor site at 6 h and 24 h after material injection. In the targeted group, the ultrasonic echo signal was greater at 24 h than at 6 h, and both the grayscale and CEUS signals were significantly greater in the targeted group than in the nontargeted group ($P < 0.05$) (Fig. 9).

Antitumor effects of the NPs in vivo

With continued treatment, the tumor volume in the model group of mice continued to increase, whereas the aPDL1-DTX/PFP@Lipid + LIPUS group exhibited a significant trend toward tumor growth inhibition. By the 14th day, the tumor growth inhibition rate reached 88.91% in the aPDL1-DTX/PFP@Lipid + LIPUS group (Fig. 10).

Pathological examination

H&E staining (Fig. 11A) revealed that the tumor cell nuclei in the control group were deeply stained, varied in size, and displayed features of nuclear division. Conversely, in the aPDL1-DTX/PFP@Lipid + LIPUS group, most tumor cell nuclei appeared condensed and necrotic, indicating potent tumor cell killing effects. Confocal laser microscopy revealed positive Pan CK expression in the epithelial cells of the PDAC tissues, which colocalized with the DAPI-labeled cell nuclei. Furthermore, there was a significant increase in CD8 + T-cell infiltration in the aPDL1-DTX/PFP@Lipid + LIPUS group ($P < 0.0001$). The expression of the antigen Ki67, which is associated with tumor cell proliferation, and α-SMA, which is linked to cancer-related fibroblasts, was markedly reduced in the aPDL1-DTX/PFP@Lipid + LIPUS group ($P < 0.0001$) (Fig. 11B-D). Immunohistochemical analysis revealed a decrease in FoxP3 and CD206 expression, whereas

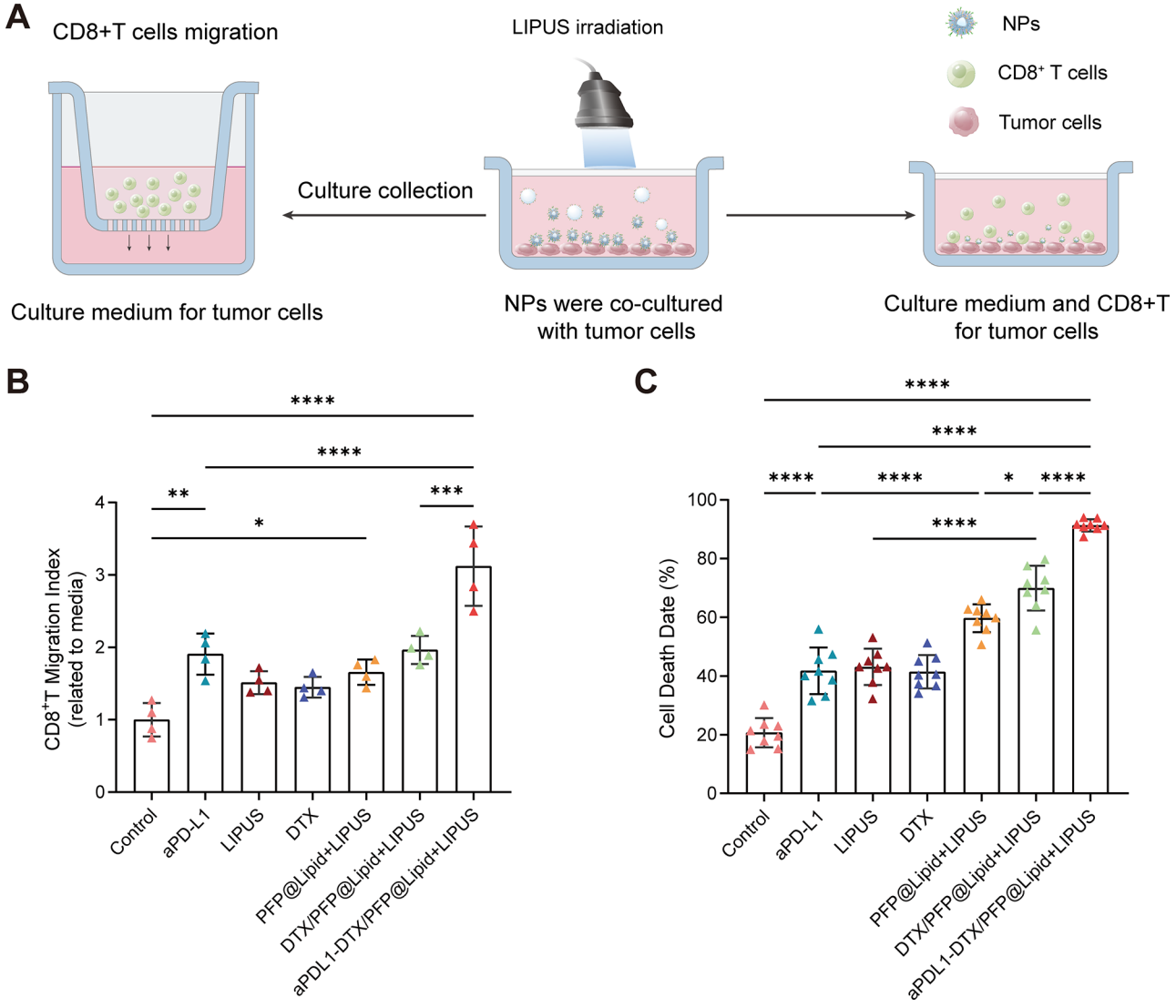

Fig. 7 Immune response of NPs *in vitro*. (**A**) In vitro recruitment of CD8 + T cells and killing of tumor cells by NPs combined with LIPUS. (**B**) Comparison of the CD8 + T-cell migration indices among the various groups. (**C**) Comparison of the CD8 + T-cell killing efficiency against Pan02 cells among the various groups

CD86 expression increased in the aPDL1-DTX/PFP@Lipid + LIPUS group (Fig. 12).

Discussion

Microbubble ultrasound contrast agents can resonate with ultrasound waves, resulting in strong backscattering and significantly amplified echoes [19, 20]. This technology has been widely utilized for clinical disease diagnosis, marking a significant advancement in ultrasound imaging, and is frequently considered the third revolution in this field. However, because the average particle size of microbubble ultrasound contrast agents currently used in clinical practice is 2.6 μm, they cannot pass through the approximately 150 nm inner diameter of endothelial gaps and extravasate from blood vessels [21, 22], which prevents their development for use in tumor-targeted molecular diagnosis. The use of liquid–vapor phase-transformation NPs represents a novel approach for further molecular ultrasound imaging of tumors. NPs are not easily visualized in B-mode or by CEUS imaging, but they can undergo a phase transformation to form MBs upon the application of ultrasound, which results in noticeable echo enhancement [23]. These smaller nanoparticles can then pass through gaps in vascular endothelial cells and, if they are endowed with specific modifications, can directly attach to tumor cells. Moreover, when nanoparticles undergo a phase change upon heating or applying ultrasound irradiation, the formed ultrasonography-visible microbubbles can be utilized for molecular tumor diagnosis.

The phase-transformation ability and targeted imaging effect of liquid–vapor phase-transformation NPs

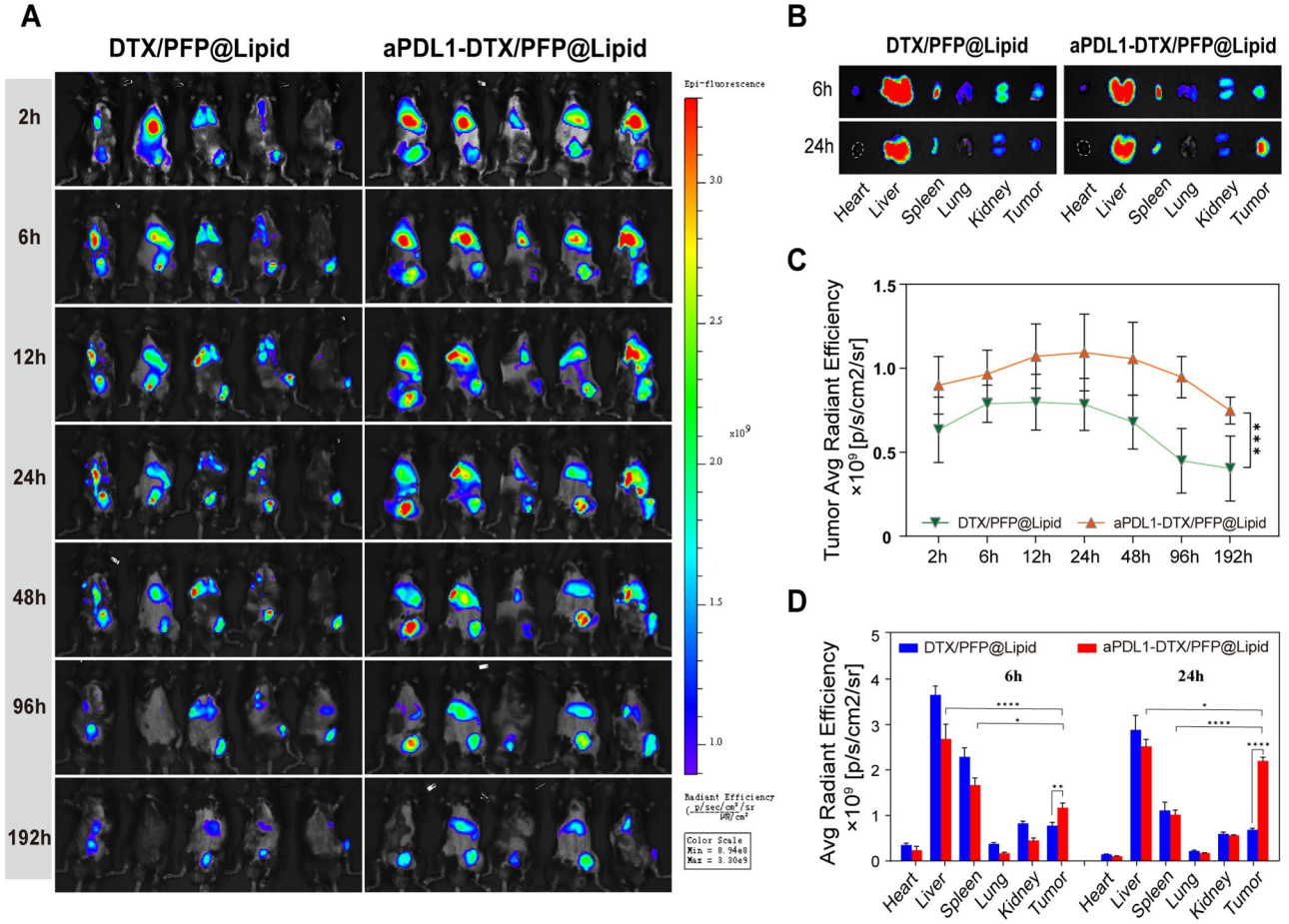

Fig. 8 Intratumoral biodistribution of the NPs. Both the targeted and nontargeted groups were iv. injected with NPs, followed by IVIS imaging of the tumors at different time points (**A**) and the corresponding time–tumor fluorescence intensity curves (**C**). Distribution of fluorescence in the major organs and excised tumors at 6 h and 24 h after intravenous injection (**B**) and the corresponding signal intensity analysis (**D**)

have been a focus of research. Many nanoparticles mentioned in the literature have relatively large particle sizes (ranging from 196.6 to 367 nm)(Supplementary Table 1), limited targeting capabilities, and suboptimal phase-transformation properties, which lead to low echo signal intensities in contrast to ultrasound. To increase the contrast ultrasound echo intensity in specific targeted tissues and achieve true molecular ultrasound diagnosis, it is essential to focus on improving the selection of nanoparticle materials, refining the preparation methods, controlling the particle size, and implementing targeted modifications.

Phospholipids are commonly selected as shell materials for lipid nanoparticles because of their favorable elasticity and ductility [24]. In this research, synthetic phospholipids were utilized for the shell, and cholesterol was added in an appropriate proportion to increase the rigidity and stability of the nanoparticles. The core of the nanoparticles contained a liquid fluorocarbon, which is crucial for achieving phase transformation [25]. The transformation in size and morphology of liquid–vapor phase-transformation nanoparticles primarily relies on the thermodynamic phase transformation of the encapsulated PFP [25]. The shift between the liquid and vapor states of PFP is contingent upon the equilibrium between the PFP liquid's vapor pressure and the surrounding pressure; when the ambient pressure exceeds the vapor pressure, PFP maintains its liquid state, and when the local surrounding pressure falls below the vapor pressure, PFP liquid molecules swiftly convert to the vapor state [26]. The vapor pressure can increase with increasing temperature of the liquid phase. Hence, when the environmental pressure surrounding PFP droplets remains constant, a transition to the vapor phase takes place once the temperature surpasses a certain threshold. For example, PFP, with a boiling point of 29 °C, transitions from liquid to gas at the body's normal temperature of 36–37 °C. However, when PFP is encapsulated within a lipid shell to form nanoparticles and dispersed in different environments (liquid or tumor tissue environments), this undoubtedly alters the local pressure around the PFP liquid core, disrupting the balance between PFP and

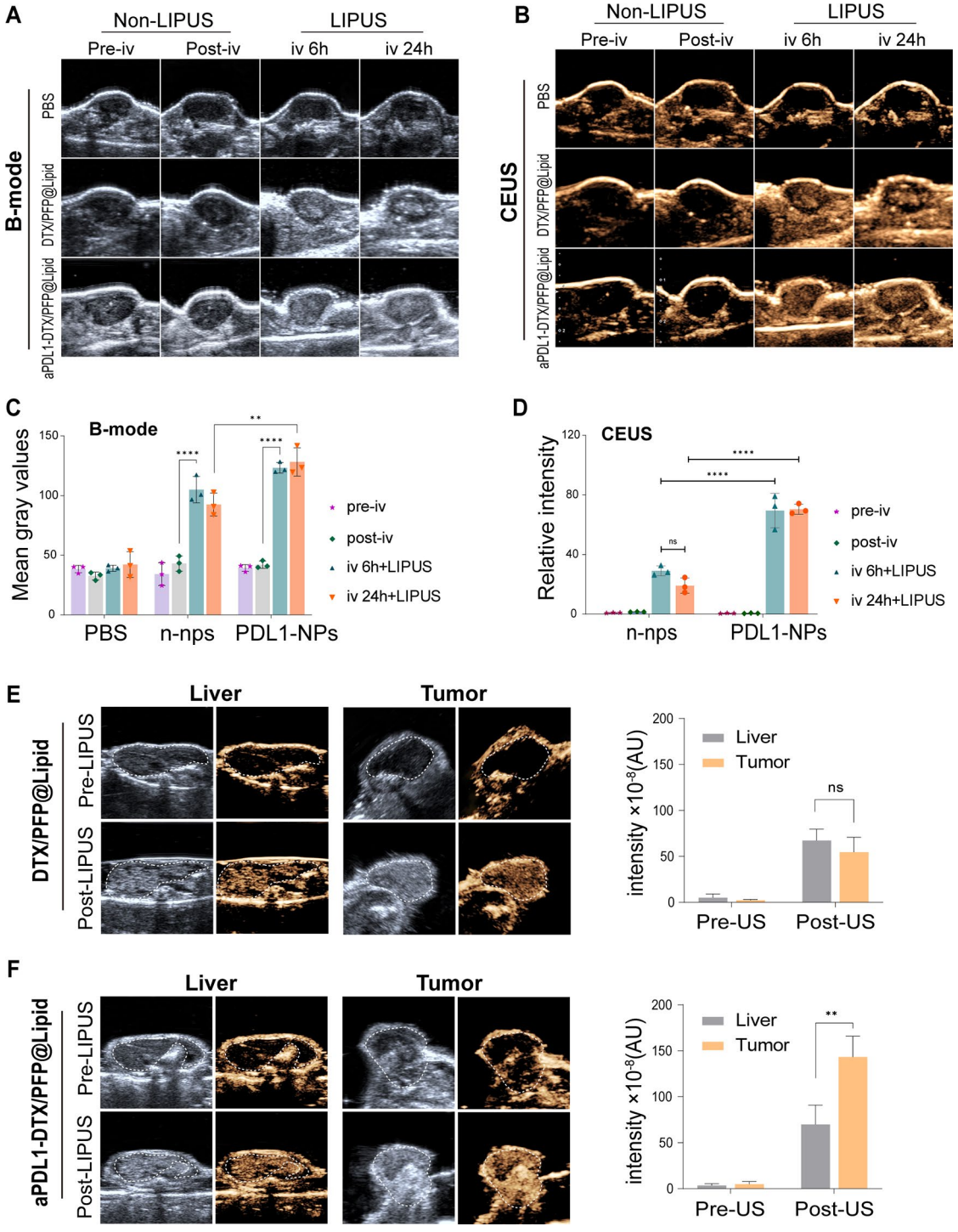

Fig. 9 In vivo phase changes in the NPs enhanced ultrasound imaging when the NPs were applied in combination with LIPUS irradiation. B-mode (**A**) and CEUS (**B**) images of tumors after intravenous injection of PBS, DTX/PFP@Lipid, or aPDL1-DTX/PFP@Lipid before and after injection combined with LIPUS irradiation 6 h and 24 h after injection. (**C**) B-mode image gray value analysis of the tumors obtained by ultrasound. (**D**) Analysis of the signal intensity of the tumor on CEUS images. Ultrasound signals in the tumors and liver 24 h after injection of DTX/PFP@Lipid (**E**) and aPDL1-DTX/PFP@Lipid (**F**) before and after LIPUS irradiation

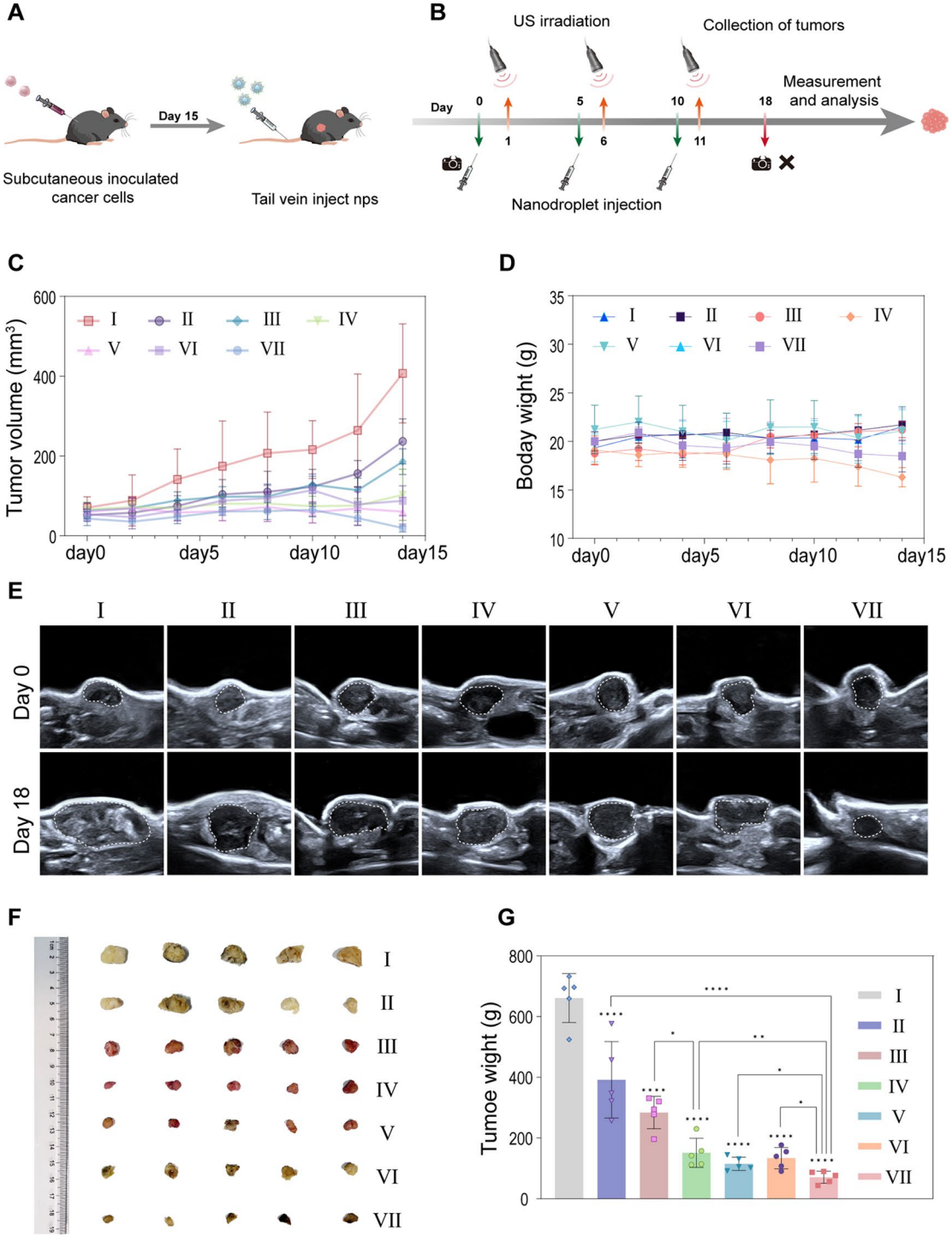

Fig. 10 Effectiveness of using NPs to combat murine PDAC. (**A**) Creation of the murine subcutaneous PDAC xenograft model. (**B**) Schematic of NPs plus LIPUS treatment for murine PDAC. Curves of mouse tumor growth (**C**) and body weights (**D**) throughout treatment. (**E**) Comparative analysis of ultrasound images of the tumor site before and after treatment. (**F**) Visual image of the remaining tumor mass. (**G**) Evaluation of residual tumor weight across different treatment groups (I. control, II. LIPUS, III. aPD-L1, IV. DTX, V. aPDL1-DTX/PFP@Lipid, VI. DTX/PFP@Lipid + LIPUS, and VII. aPDL1-DTX/PFP@Lipid + LIPUS)

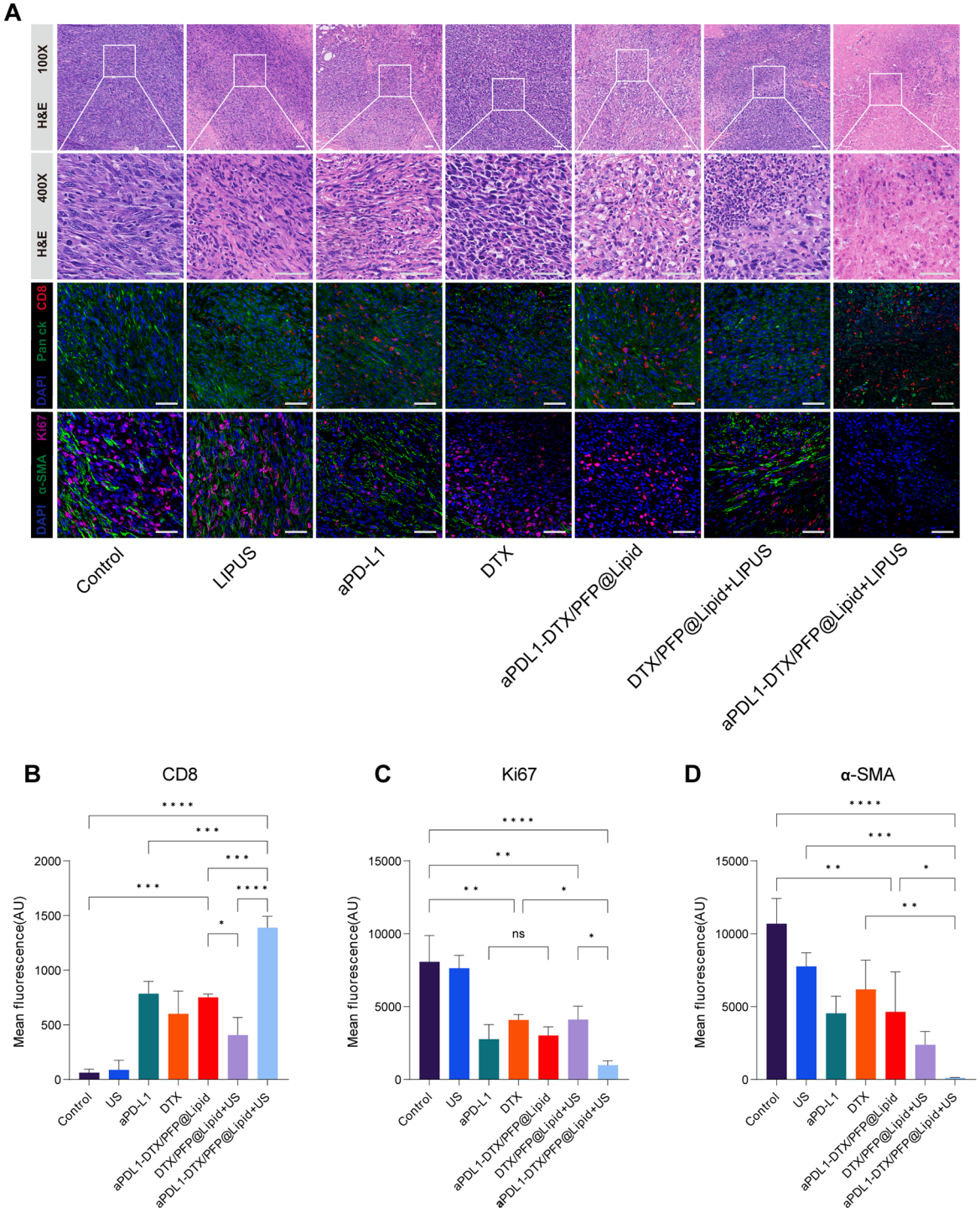

Fig. 11 Histopathological examination of tumor tissues. (**A**) Histological and immunofluorescence images of tumors from each treatment group (scale bar = 50 μm).(**B-D**) Analysis of the fluorescence intensity of CD8 + T cells and Ki67 and α-SMA marker expression

atmospheric pressure and thereby changing the conditions that trigger the morphological transformation of the nanoparticles. Additionally, the actual boiling point of PFP within the nanoparticles is greater because of the Laplace pressure [27, 28].

Research indicates that the stability of nanoparticles in solution depends on the counteracting force of the partial pressure of the dissolved gas in the surrounding fluid, the Laplace pressure, and the environmental pressure [29]. Laplace pressure is the additional pressure exerted on the fluid inside droplets or bubbles of two

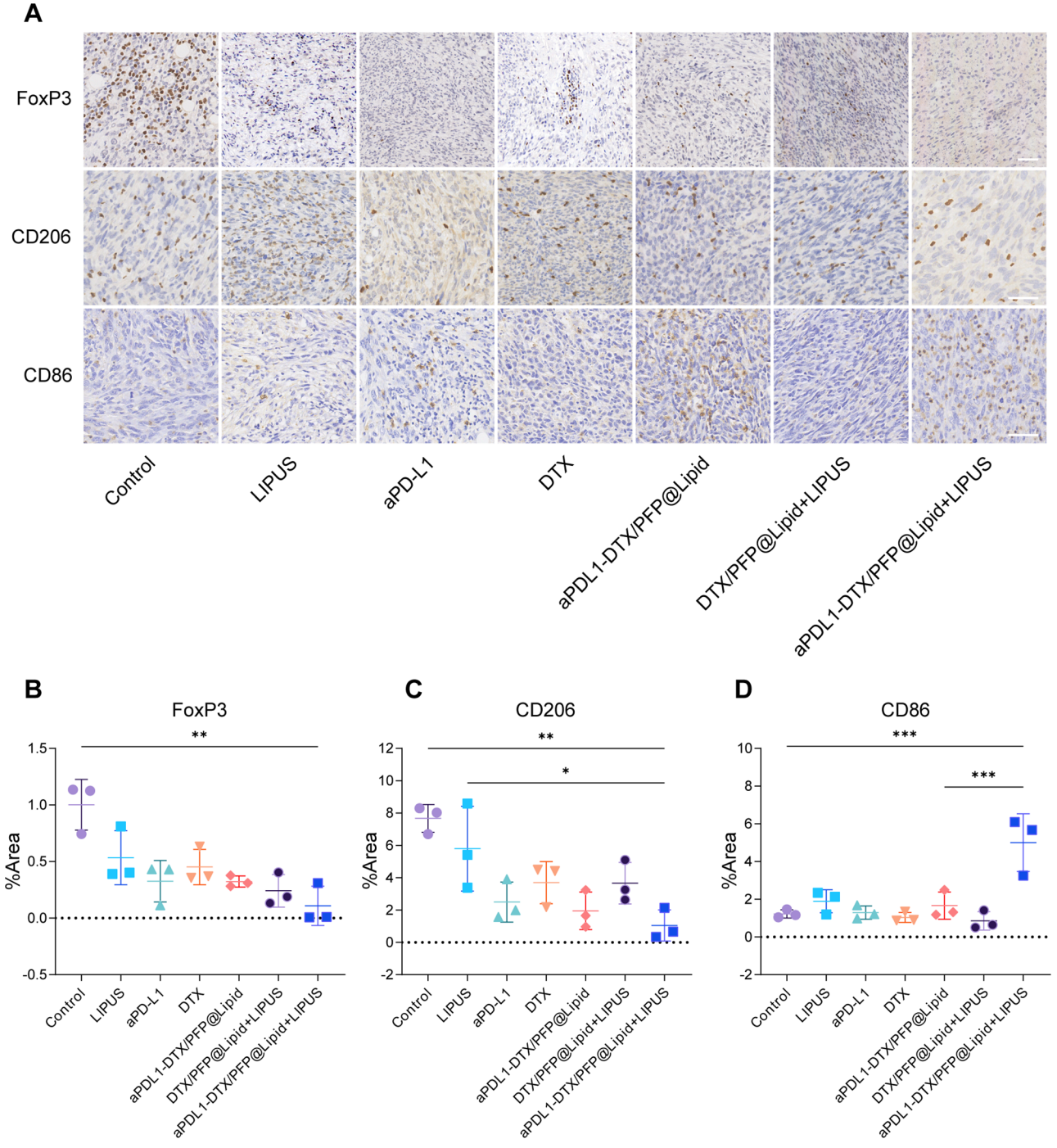

Fig. 12 Immunohistochemical analysis of tumors from each treatment group. (**A**) Microscopy images showing the expression of FoxP3, CD206, and CD86 (scale bar = 50 μm). (**B-D**) Statistical analyses of expression levels

immiscible phases due to surface tension (or interfacial energy) between the liquid or gas inside the droplet and the surrounding medium. The formula suggests the following: $\triangle P_{\text{Laplace}}=P_{\text{inside}}-P_{\text{outside}}=2\sigma/r$ (where P_{inside} is the pressure inside the droplet, P_{outside} is the pressure outside a droplet, σ is the surface tension at the droplet interface, and r is the droplet radius) [28, 30]. Laplace pressure provides additional external pressure on the PFP liquid core within the nanoparticles, the magnitude of which is related not only to the inherent surface energy of the nanoparticles (influenced by shell materials, etc.) but also inversely proportional to the radius of the nanoparticles [30, 31].This implies that smaller-sized nanoparticles can provide greater Laplace pressure on

the surface of the PFP liquid core, which requires more energy to induce vaporization, such as a higher temperature to increase the internal vapor pressure or a lower ambient pressure, thereby conferring a more stable structure on the nanoparticles. The nanoparticles produced in this study have a diameter of approximately 60 nm and a phase change temperature of 50–55 °C, which is significantly higher than the normal temperature of the human body. These features improve the stability of the nanoparticles upon intravenous injection into the bloodstream, reducing the risk of gas embolism caused by spontaneous phase changes in the nanoparticles within the circulation.

The nanoparticles were prepared by thin film hydration and ultrasonic emulsification(Supplementary Table 1) [11, 32]. Traditional ultrasonic emulsification typically involves the use of instruments such as an ultrasonic cell crusher [9, 33], which requires the insertion of a cone-shaped amplitude rod into the solution, causing the solution container to seal properly. Moreover, the high energy at the head end of the amplitude rod results in an uneven distribution of ultrasonic energy, causing a premature phase change of the liquid fluorocarbon during nanoparticle preparation and leading to variations in particle size. To address these issues, a noncontact ultrasonic crusher was employed in this study.

Phospholipids and PFP were enclosed in a centrifuge tube, and ultrasonic waves were then applied from the outside to the inside of the tube, ensuring uniform energy distribution. The closed space generates a specific pressure, which prevents the spontaneous phase change of PFP [34]. Consequently, the prepared nanoparticles contained an adequate amount of PFP that was evenly distributed. The size of the gap between cancer blood vessels has been estimated to be 100–600 nm. By adjusting the ultrasound energy and irradiation mode, nanoparticles with a particle size of less than 100 nm were obtained that could easily pass through blood vessel endothelial gaps, which ensures their good stability [35].

Guo et al. [36] reported a method for preparing liquid–vapor phase-transformation lipid nanoparticles, with EE and LC values of 82.2% and 6.85%, respectively, for paclitaxel. However, the high-energy noncontact ultrasonic emulsification method employed in this study significantly improved the EE and LC of DTX to 91.9% and 14.8%, respectively, and demonstrated good in vitro and in vivo release stability of DTX. Based on TEM images, it was inferred that DTX was primarily loaded onto the shell of the nanoparticles. In vitro storage tests of aPDL1/DTX/PFP@Lipid drug release revealed that even after continuous dialysis for 192 h, only 12.4% of the DTX was released.

After intravenous injection of free DTX, more than 98% of the DTX in the plasma is extensively bound to albumin and α1-acid glycoprotein [37] and is then metabolized primarily by the cytochrome P450 (CYP) 3A4 system in the liver and excreted into the feces via bile [38, 39]. Studies have reported that most of the DTX-loaded lipid nanoparticles administered intravenously are taken up by reticuloendothelial cells in the liver, spleen, and other areas [40] and that DTX can be continuously released from the lipid carrier, thereby extending the metabolic time [41]. The results of this study show that after intravenous injection of aPDL1/DTX/PFP@Lipid into the tail vein of normal rats without a tumor burden, the amount of DTX in the plasma accounted for approximately 0.9% of the total amount loaded after 1 h, which was lower than the amount released in vitro, possibly related to the redistribution of some nanoparticles in tissues. Within 6 h, as free DTX is rapidly cleared and lipid drug-loaded nanoparticles complete tissue biodistribution [42], DTX in the peripheral blood decreases rapidly, reaches equilibrium at 24 h, and is maintained at a low level for several days thereafter.

Currently, the two primary methods widely used for droplet phase change are heating and ADV [26, 28]. ADV refers to the physical process where phase-transformation droplets, typically containing a perfluorocarbon core, undergo a phase transformation from a liquid to a gaseous state when subjected to sufficient acoustic pressures. ADV utilizes ultrasonic irradiation, which offers a high penetration depth and controllable energy, increasing its practicality [43]. ADV-mediated nanoparticle vaporization is influenced by various factors, such as nanoparticle interfacial tension, size, ultrasound frequency, and pressure amplitude [44]. Lipid shells exhibit excellent mechanical elasticity, allowing for repeated expansion and contraction [45], along with high biocompatibility, good loading capacity, and controllable biological properties [46, 47]. The energy required to reach the vaporization threshold of phase-transformation nanoparticles increases proportionally with the length of the lipid acyl chain, and the lipid composition modulates the acoustic characteristics of the nanodroplets [24, 48]. On the other hand, cholesterol maintains relatively stable biofilm fluidity across various temperatures without significantly impacting the phase change temperature, thus increasing the stiffness of the phase-transformation nanoparticles.

Ultrasound propagates through a medium by alternately generating regions of compression (high-density areas) and rarefaction (low-density areas), causing local pressure fluctuations between positive and negative pressures. The amplitude of these vibrations indicates the absolute value of the pressure intensity. During the negative pressure phase of the alternating cycle of sound waves, the environmental pressure around the NPs decreases (decompression phase), and there is a driving force for the formation of a gas phase (amplitude

intensity) within this interval. The greater the amplitude intensity of the sound wave is, the more pronounced the driving force. When the sum of the driving force and Laplace pressure remains below the internal vapor pressure, PFP vaporization causes the nanoparticle to expand in volume into a microbubble [44]. LIPUS has a lower frequency and longer pulse intervals, thus providing a longer decompression phase to ensure that the nanoparticles have ample time to undergo phase transformation. The microbubbles produced after the phase transformation of the nanoparticles create a significant acoustic impedance difference from that of the surrounding tissue, thereby enhancing the ultrasound imaging signal.

When the incident ultrasound frequency matches the natural oscillation frequency of the microbubble, resonance occurs, resulting in the highest acoustic energy output and optimal CUES performance. The resonant frequency is inversely correlated with the microbubble diameter; for example, a 3 μm microbubble resonates at 2.4 MHz, whereas a 5 μm microbubble resonates at 1.3 MHz. The conversion of PFP from a liquid to a gas causes a volume expansion of approximately 125 times. If the particle size of a prepared nanoparticle exceeds 200 nm, its extravasation from blood vessels for effective targeting and binding to tumor cells may be hindered. On the other hand, after phase transformation, the MBs size can reach 25 μm, exceeding the resonant frequency of diagnostic ultrasound commonly used in clinical settings and potentially compromising the efficacy of ultrasound imaging. In the experiments here, the NPs transition to MBs led to a 120-fold expansion in vitro to approximately 7 μm. In vivo, considering constraints such as interstitial pressure, the size of the MBs was controlled and closely mimicked that of traditional ultrasound contrast agents. This enhancement facilitates an up to 125-fold increase in echo intensity for effective nanoparticle-mediated contrast-enhanced molecular ultrasound diagnosis.

Following intravenous injection, the NPs are readily cleared by the reticuloendothelial system in vivo. The aim of this study was to reduce uptake by reticuloendothelial cells in vivo by adding PEG to the nanoparticle shell and controlling the nanoparticle size [49]. Additionally, an aPD-L1 antibody was conjugated to the NPs surface via carbodiimide chemistry, enabling targeted binding to PDAC cells expressing PD-L1. Fluorescence imaging analysis demonstrated enhanced binding of the NPs to PDAC cells, particularly those at the tumor site.

The unique and complex immune TME of PDAC contributes to unfavorable clinical treatment outcomes and prognosis [50]. This research demonstrated that intravenous nanoparticle injection led to significant antitumor effects in mice with PDAC. This treatment regimen resulted in a significant decrease in α-SMA expression, which is linked to cancer-associated fibroblasts and fibroplasia inhibition in cancerous tissues. The PD-L1 antibody-modified NPs not only displayed targeting effects but also blocked the PD-L1/PD-1 pathway in PDAC, thereby reducing immune suppression and restoring the cytotoxic effect of effector T cells [51, 52]. In vitro CD8 + T-cell chemotaxis and tumor cell killing experiments revealed that the tumor microenvironment after aPDL1-DTX/PFP@Lipid combined with LIPUS irradiation not only increases the recruitment efficiency of CD8 + T cells but also enhances the cytotoxic effect of CD8 + T cells in conjunction with nanoparticles on tumor cells. Following nanoparticle administration, fewer Treg cells (FoxP3+) and M2 macrophages (CD206+) are present in PDAC tissues, along with more CD8 + T cells and M1 macrophages (CD86+) at the tumor site, which remodel the PDAC immune microenvironment to a certain extent [13, 50, 53]. Additionally, the release of oxygen from the PFP core of the nanoparticles improved the hypoxic conditions in the PDAC microenvironment [36, 54, 55].

Liquid–vapor phase-transformation NPs have been shown to bind specifically to PDAC cells, and these NPs experience transient changes in size during ADV. MBs, under the influence of LIPUS pressure waves, alternately expand and contract, generating linear and nonlinear oscillations until they reach their maximum size and eventually rupture. This process results in the formation of microjets and shock waves, similar to the effects of UTMD, and the resulting shear forces can increase the permeability of the cell membrane [56]. Additionally, the instantaneous energy released when MBs burst leads to acoustic cavitation effects, further disrupting the cell membrane and allowing for increased drug entry into the cells [57]. DTX has poor water solubility and high systemic toxicity when it is administered systemically. However, by encapsulating DTX in targeted nanobubbles and applying UTMD, these limitations can be overcome, ultimately enhancing the antitumor effects of DTX.

Conclusion

In this study, targeted drug-loaded liquid–vapor phase-transformation nanoparticles, aPDL1-DTX/PFP@Lipid NPs, which possess an optimal particle size that enables them to penetrate vascular endothelial cell gaps and bind specifically to PDAC cells, were developed. Upon ultrasound irradiation, these NPs undergo a phase change, transforming into MBs that exhibit strong diagnostic ultrasound resonance to significantly enhance the ultrasound imaging efficacy and enable targeted molecular ultrasound diagnosis of PDAC. Furthermore, the biological effects induced by the ultrasound-mediated disruption of the microbubbles increased the permeability of the PDAC cell membranes, facilitating drug penetration into the cells. The combination of UTMD, PD-L1

antibodies and DTX effectively inhibits PDAC cells and reshapes the TME through mechanisms such as suppressing fibrous tissue proliferation, reversing immune suppression, and ameliorating hypoxia. This approach allows the precise targeted diagnosis and treatment of PDAC through molecular ultrasound imaging and shows considerable potential for clinical application.

Abbreviations

ADV	Acoustic droplet vaporiztion
aPD-L1	Anti-PD-L1 antibody
aPDL1-DTX/PFP@Lipid	aPD-L1-modified docetaxel and perfluoropentane-loaded liquid–vapor phase-transformation lipid nanoparticles
CEUS	Contrast-enhanced ultrasound
DSPC	1,2-distearoyl-sn-glycero-3-phosphocholine
DSPE-PEG_{2000}	1,2-distearoyl-sn-glycero-3-phosphoethanolamine-N–[methoxy(ethylene glycol)-2000
DSPE-PEG_{2000}-COOH	1,2-distearoyl-sn-glycero-3-phosphoethanolamine-N-[carboxy(polyethylene glycol)-2000
DTX	Docetaxel
DTX/PFP@Lipid	Docetaxel and perfluoropentane-loaded liquid–vapor phase-transformation lipid nanoparticles
EDC	Ethyl-3-(3-dimethyl-aminopropyl) carbodiimide
EE	Encapsulation efficiency
LC	Loading capacity
LIPUS	Low-intensity pulsed ultrasound
MBs	Microbubbles
NPs	Nanoparticles
NHS	N-hydroxysuccinimide
PBS	Phosphate-buffered saline
PDAC	Pancreatic ductal adenocarcinoma
PFP	Perfluoropentane
PFP@Lipid	Perfluoropentane-loaded liquid–vapor phase-transformation lipid nanoparticles
ROS	Reactive oxygen species
TME	Tumor microenvironment
UTMD	Ultrasound-targeted microbubble destruction

Supplementary Information

The online version contains supplementary material available at https://doi.org/10.1186/s12951-025-03105-7.

Supplementary Material 1

Acknowledgements

We thank the members of the Fujian Institute of Ultrasonic Medicine for their helpful comments and suggestions. The authors thank the Public Technology Service Center Fujian Medical University and the Central Laboratory of Union Hospital affiliated with Fujian Medical University for their help and technical support.

Author contributions

Z.C. was involved in the design, planning, experimental guidance, funding support, and final decision-making of the entire research; Y.T. and Q. S.were directly involved in the research design, experimental progress, and writing; P.L. provided experimental design direction and revised the manuscript; Z.C. and D.F. supplemented some experimental data; M.Z. analyzed the data and prepared the schematic diagramt; Y.G. wrote the manuscript; Y.S. assisted with data search and organizing; Q.Q.provided technical assistance in material construction; L.L. participated in project design guidance; E.X.provided financial support for publishing the paper; All authors reviewed and edited the manuscript.

Funding

This research was supported by Joint Funds for the Innovation of Science and Technology, Fujian Province (Grant number: 2019Y9066).

Data availability

No datasets were generated or analysed during the current study.

Declarations

Ethics approval and consent to participate

Animal care was performed in accordance with institutional institution guidelines. All animal studies were approved by the Animal Ethical Committee of Fujian Medical University (grant No. IACUC FJMU 2022 – 0721).

Consent for publication

Not applicable.

Competing interests

The authors declare no competing interests.

Author details

[1]Department of Ultrasound, Fujian Medical University Union Hospital, 29 Xinquan Road, Fuzhou, China
[2]Fujian Institute of Ultrasonic Medicine Laboratory, 29 Xinquan Road, Fuzhou, China
[3]Fujian College Association Instrumental Analysis Center, Fuzhou University, 2 Xueyuan Road, Fuzhou, China
[4]Department of General Surgery, Affiliated Zhongshan Hospital of Dalian University, No. 6 Jiefang Street, Zhongshan District, Dalian, China

Received: 26 July 2024 / Accepted: 10 January 2025
Published online: 28 January 2025

References

1. Siegel RL, Miller KD, Wagle NS, Jemal A. Cancer statistics, 2023. Cancer J Clin. 2023;73:17–48.
2. [Internet] American Cancer Society. Key Statistics for Pancreatic Cancer. Revised February 5,2024.https://cancerstatisticscenter.cancer.org/
3. Sherman MH, Beatty GL. Tumor microenvironment in pancreatic cancer pathogenesis and therapeutic resistance. Annu Rev Pathol. 2023;18:123–48.
4. Zeng H, Chen W, Zheng R, Zhang S, Ji JS, Zou X, et al. Changing cancer survival in China during 2003-15: a pooled analysis of 17 population-based cancer registries. Lancet Global Health. 2018;6:e555–67.
5. Sontum PC. Physicochemical characteristics of Sonazoid, a new contrast agent for ultrasound imaging. Ultrasound Med Biol.2008;34:824–833.
6. Barua S, Mitragotri S. Challenges associated with penetration of nanoparticles across cell and tissue barriers: a review of current status and future prospects. Nano Today. 2014;9:223–43.
7. Rowe SP, Pomper MG. Molecular imaging in oncology: current impact and future directions. Cancer J Clin. 2022;72:333–52.
8. Xuan Y, Guan M, Zhang S. Tumor immunotherapy and multi-mode therapies mediated by medical imaging of nanoprobes. Theranostics. 2021;11:7360–78.
9. Liu Z, Ran H, Wang Z, Zhou S, Wang Y. Targeted and pH-facilitated theranostic of orthotopic gastric cancer via phase-transformation doxorubicin-encapsulated nanoparticles enhanced by low-intensity focused ultrasound (LIFU) with reduced side effect. Int J Nanomed. 2019;14:7627–42.
10. Yang C, Zhang Y, Luo Y, Qiao B, Wang X, Zhang L, et al. Dual ultrasound-activatable nanodroplets for highly-penetrative and efficient ovarian cancer theranostics. J Mater Chem B. 2020;8:380–90.
11. Yu M, Xu X, Cai Y, Zou L, Shuai X. Perfluorohexane-cored nanodroplets for stimulations-responsive ultrasonography and O2-potentiated photodynamic therapy. Biomaterials. 2018;175:61–71.
12. Wu N, Cao Y, Liu Y, Zhou Y, He H, Tang R, et al. Low-intensity focused ultrasound targeted microbubble destruction reduces tumor blood supply and sensitizes anti-PD-L1 immunotherapy. Front Bioeng Biotechnol. 2023;11:1173381.
13. Zheng J, Huang J, Zhang L, Wang M, Xu L, Dou X, et al. Drug-loaded microbubble delivery system to enhance PD-L1 blockade immunotherapy with remodeling immune microenvironment. Biomaterials Res. 2023;27:9.

14. Ye D, Yuan J, Yue Y, Rubin JB, Chen H. Focused ultrasound-enhanced delivery of intranasally administered anti-programmed cell death-ligand 1 antibody to an intracranial murine glioma model. Pharmaceutics. 2021;13:190.
15. Emami F, Duwa R, Banstola A, Woo SM, Kwon TK, Yook S. Dual receptor specific nanoparticles targeting EGFR and PD-L1 for enhanced delivery of docetaxel in cancer therapy. Biomed Pharmacother. 2023;165:115023.
16. Du Y, Wang Z, Wang T, He W, Zhou W, Li M, et al. Improved Antitumor Activity of Novel Redox-Responsive Paclitaxel-Encapsulated liposomes based on Disulfide Phosphatidylcholine. Mol Pharm. 2020;17:262–73.
17. Tantipolphan R, Rades T, McQuillan AJ, Medlicott NJ. Adsorption of bovine serum albumin (BSA) onto lecithin studied by attenuated total reflectance Fourier transform infrared (ATR-FTIR) spectroscopy. Int J Pharm. 2007;337:40–7.
18. Xin L, Zhang C, Chen J, Jiang Y, Liu Y, Jin P, et al. Ultrasound-Activatable Phase-Shift Nanoparticle as a Targeting Antibacterial Agent for efficient eradication of Pseudomonas aeruginosa Biofilms. ACS Appl Mater Interfaces. 2022;14:47420–31.
19. Helfield B. A review of Phospholipid Encapsulated Ultrasound contrast Agent Microbubble Physics. Ultrasound Med Biol. 2019;45:282–300.
20. Yusefi H, Helfield B. Subharmonic resonance of phospholipid coated ultrasound contrast agent microbubbles. Ultrason Sonochem. 2024;102:106753.
21. Danquah MK, Zhang XA, Mahato RI. Extravasation of polymeric nanomedicines across tumor vasculature. Adv Drug Deliv Rev. 2011;63:623–39.
22. Maruyama K. Intracellular targeting delivery of liposomal drugs to solid tumors based on EPR effects. Adv Drug Deliv Rev. 2011;63:161–9.
23. Liu J, Shang T, Wang F, Cao Y, Hao L, Ren J, et al. Low-intensity focused ultrasound (LIFU)-induced acoustic droplet vaporization in phase-transition perfluoropentane nanodroplets modified by folate for ultrasound molecular imaging. Int J Nanomedicine. 2017;12:911–923.
24. Chattaraj R, Goldscheitter GM, Yildirim A, Goodwin AP. Phase behavior of mixed lipid monolayers on Perfluorocarbon nanoemulsions and its Effect on Acoustic contrast. RSC Adv. 2016;6:111318–25.
25. Zhang W, Metzger H, Vlatakis S, Claxton A, Carbajal MA, Fung LF, et al. Characterising the chemical and physical properties of phase-change nanodroplets. Ultrason Sonochem. 2023;97:106445.
26. Lin C-Y, Pitt WG. Acoustic droplet vaporization in biology and medicine. Biomed Res Int. 2013; 2013: 404361.
27. Matsunaga TO, Sheeran PS, Luois S, Streeter JE, Mullin LB, Banerjee B, Dayton PA. Phase-change nanoparticles using highly volatile perfluorocarbons: toward a platform for extravascular ultrasound imaging. Theranostics. 2012;2:1185–98.
28. Kee ALY, Teo BM. Biomedical applications of acoustically responsive phase shift nanodroplets: current status and future directions. Ultrason Sonochem. 2019;56:37–45.
29. Perera RH, Hernandez C, Zhou H, Kota P, Burke A, Exner AA. Ultrasound imaging beyond the vasculature with new generation contrast agents. Wiley Interdiscip Rev Nanomed Nanobiotechnol. 2015;7:593–608.
30. Qin D, Zou Q, Lei S, Wang W, Li Z. Predicting initial nucleation events occurred in a metastable nanodroplet during acoustic droplet vaporization. Ultrason Sonochem. 2021;75:105608.
31. Rapoport N. Phase-shift, stimuli-responsive perfluorocarbon nanodroplets for drug delivery to cancer. Wiley Interdiscip Rev Nanomed Nanobiotechnol. 2012;4:492–510.
32. Ferri S, Wu Q, De Grazia A, Polydorou A, May JP, Stride E, et al. Tailoring the size of ultrasound responsive lipid-shelled nanodroplets by varying production parameters and environmental conditions. Ultrason Sonochem. 2021;73:105482.
33. Zhao H, Wu M, Zhu L, Tian Y, Wu M, Li Y, et al. Cell-penetrating peptide-modified targeted drug-loaded phase-transformation lipid nanoparticles combined with low-intensity focused Ultrasound for Precision Theranostics against Hepatocellular Carcinoma. Theranostics. 2018;8:1892–910.
34. Sheeran PS, Luois SH, Mullin LB, Matsunaga TO, Dayton PA. Design of ultrasonically activatable nanoparticles using low boiling point perfluorocarbons. Biomaterials. 2012;33:3262–9.
35. Li M, Liu Y, Zhang Y, Yu N, Li J. Sono-Activatable Semiconducting Polymer nanoreshapers Multiply Remodel Tumor Microenvironment for Potent Immunotherapy of Orthotopic Pancreatic Cancer. Volume 10. Baden-Wurttemberg, Germany: Advanced Science (Weinheim; 2023. p. e2305150.
36. Guo X, Tu P, Zhu L, Cheng C, Jiang W, Du C, et al. Nanoenabled Tumor Energy Metabolism Disorder via Sonodynamic Therapy for Multidrug Resistance Reversal and Metastasis Inhibition. ACS Appl Mater Interfaces. 2023;15:309–26.
37. Urien S, Barré J, Morin C, Paccaly A, Montay G, Tillement JP. Docetaxel serum protein binding with high affinity to alpha 1-acid glycoprotein. Invest New Drugs. 1996;14:147–51.
38. Clarke SJ, Rivory LP. Clinical pharmacokinetics of docetaxel. Clin Pharmacokinet. 1999;36:99–114.
39. Paolini M, Poul L, Berjaud C, Germain M, Darmon A, Bergère M, et al. Nanosized cytochrome P450 3A4 inhibitors to block hepatic metabolism of docetaxel. Int J Nanomed. 2017;12:5537–56.
40. Zhang H, Li R-y, Lu X, Mou Z-z. Lin G-m. docetaxel-loaded liposomes: preparation, pH sensitivity, pharmacokinetics, and tissue distribution. J Zhejiang Univ Sci B. 2012;13:981–9.
41. Zhao X, Zhao Y, Geng L, Li X, Wang X, Liu Z, et al. Pharmacokinetics and tissue distribution of docetaxel by liquid chromatography–mass spectrometry: evaluation of folate receptor-targeting amphiphilic copolymer modified nanostructured lipid carrier. J Chromatogr B Analyt Technol Biomed Life Sci. 2011;879:3721–7.
42. Zhao X, Bi K, Wang X, Xue X, He B, Cui Y, et al. A UFLC-MS/MS method coupled with one-step protein precipitation for determination of docetaxel in rat plasma: comparative pharmacokinetic study of modified nanostructured lipid carrier. J Pharm Biomed Anal. 2013;83:202–8.
43. Shpak O, Verweij M, Vos HJ, de Jong N, Lohse D, Versluis M. Acoustic droplet vaporization is initiated by superharmonic focusing. Proc Natl Acad Sci USA. 2014;111:1697–702.
44. Pitt WG, Singh RN, Perez KX, Husseini GA, Jack DR. Phase transitions of perfluorocarbon nanoemulsion induced with ultrasound: a mathematical model. Ultrason Sonochem. 2014;21:879–91.
45. Sheeran PS, Matsuura N, Borden MA, Williams R, Matsunaga TO, Burns PN, Dayton PA. Methods of Generating Submicrometer phase-shift perfluorocarbon droplets for applications in Medical Ultrasonography. IEEE Trans Ultrason Ferroelectr Freq Control. 2017;64:252–63.
46. van Rooij T, Daeichin V, Skachkov I, de Jong N, Kooiman K. Targeted ultrasound contrast agents for ultrasound molecular imaging and therapy. International Journal of Hyperthermia: the Official Journal of European Society For Hyperthermic Oncology, North American Hyperthermia Group. 2015; 31.
47. Mitchell MJ, Billingsley MM, Haley RM, Wechsler ME, Peppas NA, Langer R. Engineering precision nanoparticles for drug delivery. Nat Rev Drug Discovery. 2021;20:101–24.
48. Welch PJ, Li DS, Forest CR, Pozzo LD, Shi C. Perfluorocarbon nanodroplet size, acoustic vaporization, and inertial cavitation affected by lipid shell composition in vitro. J Acoust Soc Am. 2022;152:2493.
49. Yarmoska SK, Yoon H, Emelianov SY. Lipid Shell Composition Plays a critical role in the stable size reduction of Perfluorocarbon Nanodroplets. Ultrasound Med Biol. 2019;45:1489–99.
50. Bockorny B, Grossman JE, Hidalgo M. Facts and hopes in Immunotherapy of Pancreatic Cancer. Clin Cancer Research: Official J Am Association Cancer Res. 2022;28:4606–17.
51. Brahmer JR, Tykodi SS, Chow LQM, Hwu W-J, Topalian SL, Hwu P, et al. Safety and activity of anti-PD-L1 antibody in patients with advanced cancer. N Engl J Med. 2012;366:2455–65.
52. Guo J, Zhao W, Xiao X, Liu S, Liu L, Zhang L, et al. Reprogramming exosomes for immunity-remodeled photodynamic therapy against non-small cell lung cancer. Bioactive Mater. 2024;39:206–23.
53. Wei F, Fang R, Lyu K, Liao J, Long Y, Yang J, et al. Exosomal PD-L1 derived from head and neck squamous cell carcinoma promotes immune evasion by activating the positive feedback loop of activated regulatory T cell-M2 macrophage. Oral Oncol. 2023;145:106532.
54. Zhang Y, Liao Y, Tang Q, Lin J, Huang P. Biomimetic nanoemulsion for synergistic photodynamic-immunotherapy against hypoxic breast tumor. Angewandte Chemie (International Ed English). 2021;60:10647–53.
55. Li M, Zhu Y, Yang C, Yang M, Ran H, Zhu Y, Zhang W. Acoustic triggered nanobomb for US imaging guided sonodynamic therapy and activating antitumor immunity. Drug Delivery. 2022;29:2177–89.
56. Fan C-H, Lin Y-T, Ho Y-J, Yeh C-K. Spatial-temporal Cellular Bioeffects from Acoustic Droplet vaporization. Theranostics. 2018;8:5731–43.
57. Han Y, Sun J, Wei H, Hao J, Liu W, Wang X. Ultrasound-targeted Microbubble Destruction: Modulation in the Tumor Microenvironment and Application in Tumor Immunotherapy. Front Immunol. 2022;13:937344.

Publisher's note